PHYSICS-INFORMED AUDIO-GEOMETRY-GRID REPRESENTATION LEARNING FOR UNIVERSAL SOUND SOURCE LOCALIZATION

Anonymous authors
Paper under double-blind review

ABSTRACT

Sound source localization (SSL) is a fundamental task for spatial audio understanding, yet most deep neural network-based methods are constrained by fixed array geometries and predefined directional grids, limiting generalizability and scalability. To address these issues, we propose *audio-geometry-grid representation learning* (AGG-RL), a novel framework that jointly learns audio-geometry and grid representations in a shared latent space, enabling both geometry-invariant and grid-flexible SSL. Moreover, to enhance generalizability and interpretability, we introduce two physics-informed components: a *learnable non-uniform discrete Fourier transform* (LNuDFT), which optimizes the dense allocation of frequency bins in a non-uniform manner to emphasize informative phase regions, and a *relative microphone positional encoding* (rMPE), which encodes relative microphone coordinates in accordance with the nature of inter-channel time differences. Experiments on synthetic and real datasets demonstrate that AGG-RL achieved superior performance, particularly under unseen conditions. The results highlight the potential of representation learning with physics-informed design towards a universal solution for spatial acoustic scene understanding across diverse scenarios.

1 INTRODUCTION

With the growing interest in learning and reasoning about 3D space in machine learning (Mildenhall et al., 2021; Zhang et al., 2025; Xie et al., 2025), multichannel audio has emerged as a promising modality for capturing spatial cues and enabling spatially aware generation (Ochiai et al., 2017; Simeoni et al., 2019; Richard et al., 2021; Leng et al., 2022; Luo et al., 2022; Huang et al., 2023; Zheng et al., 2024; Sun et al., 2025; Brunetto et al., 2025; Li et al., 2025a; Liang et al., 2025). A central task in this field is *sound source localization* (SSL), which estimates the direction-of-arrival (DOA) of sound sources. SSL is not only a fundamental building block in spatial audio processing but also synergizes with applications such as robotics (Gan et al., 2020; Wang et al., 2021; Do et al., 2022; Wang et al., 2024a), autonomous vehicles (Furletov et al., 2021; Jeon et al., 2025), drones (Wang & Cavallaro, 2022; Chevtchenko et al., 2025), and immersive AR/VR systems and smart devices (Rajguru et al., 2022; Gupta et al., 2022; Lin et al., 2024; Yang et al., 2025).

Traditionally, SSL has relied on classical signal processing methods based on the time difference-of-arrival (TDOA) between microphones in a microphone array (MA) (Benesty et al., 2008), such as GCC-PHAT (Knapp & Carter, 1976), MUSIC (Schmidt, 1986), and SRP-PHAT (Dibiase, 2000), which exploit inter-channel phase differences (IPDs) in the frequency domain. The advent of deep neural networks (DNNs) has enabled models to learn robust audio representations, often surpassing classical methods (Grumiaux et al., 2022; Chakrabarty & Habets, 2019; Nguyen et al., 2020; Yang et al., 2021; Diaz-Guerra et al., 2021a; He et al., 2021; Baek et al., 2023; Zhang et al., 2024; Battula et al., 2025; Li et al., 2025b). However, most existing DNN-based methods remain critically limited: they are highly dependent on specific MA geometries and predefined DOA grids.

To address these limitations, geometry-invariant SSL methods (Schwartz et al., 2023; Grinstein et al., 2024; Wang et al., 2024b; Baek et al., 2025) and grid-flexible approaches (Yang et al., 2021; Wang et al., 2024b) have been proposed. Although these methods alleviate some constraints, they still fall short of achieving robust SSL across arbitrary geometries and grids. Therefore, we propose *audio-*

geometry-grid representation learning (AGG-RL) for robust, universal SSL. Inspired by representation learning (Bengio et al., 2013; Koyama et al., 2024a; Shi et al., 2022; Dimitriadis et al., 2023; Zhu et al., 2024; Kim et al., 2025), AGG-RL learns two types of representations: audio-geometry representations (AGRs) and grid representations (GRs). AGRs are derived from audio and MA geometry, while GRs encode candidate DOA grids. Their similarity produces a probabilistic spatial spectrum, and is trained with soft labels that represent relationships among neighboring grid points. This enables the model to capture audio-geometry-grid relationships, facilitating universal SSL on arbitrary grids and geometries without retraining.

Furthermore, to enhance generalization, we introduce two components inspired by physics-informed DNNs (Raissi et al., 2019; Karniadakis et al., 2021; Gabrielli et al., 2018; Koyama et al., 2024b; Ribeiro et al., 2024; Miotello et al., 2024; Karakonstantis et al., 2024; Damiano et al., 2025): a *learnable non-uniform discrete Fourier transform* (LNuDFT) and a *relative microphone positional encoding* (rMPE). For the proposed LNuDFT, the gap between adjacent frequency bins is modeled as a learnable parameter, allowing the DNN to densely allocate bins in critical frequency regions that convey physically informative phase cues. In addition, based on absolute MPE (aMPE) (Baek et al., 2025), rMPE is introduced to embed microphone coordinates in a relative fashion—consistent with the nature of TDOA, which depends on relative rather than absolute coordinates. Both components incorporate physics-based structural assumptions into the feature extraction process while still allowing adaptivity through training. This yields physics-informed inductive biases that guide learning toward acoustically meaningful representations.

Experiments on both synthetic and real datasets (Löllmann et al., 2018) demonstrate the effectiveness of the proposed method, showing strong generalization to unseen environments in terms of angular error and accuracy. Moreover, our framework supports flexible grid selection without retraining, enhancing adaptability across diverse scenarios. These results highlight AGG-RL, augmented with LNuDFT and rMPE, as a promising step toward 3D acoustic scene understanding.

2 Background

2.1 Time Difference-of-Arrival and Inter-Channel Phase Difference

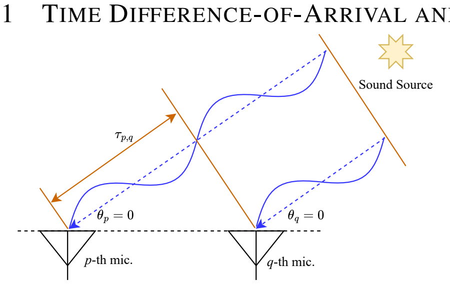

(a) Sound received by the microphone array.

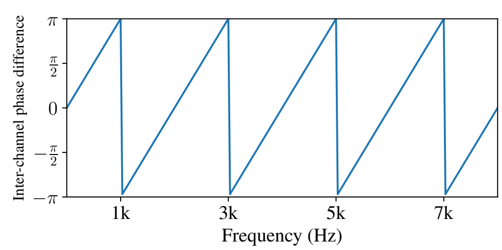

(b) IPD at $\tau = 0.5$ ms, showing phase wrapping and aliasing.

Figure 1: Illustration of (a) signals received by a microphone array and (b) IPD in the frequency domain, where phase wrapping can cause spatial aliasing.

Modeling a sound wave as a plane wave in the far-field situation, when the wave reaches spatially separated microphones at different times, a TDOA arises, as shown in Fig. 1(a). In the frequency domain, the TDOA $\tau_{p,q}$ between channels p and q is related to the IPD $\Delta\theta$ at frequency f as follows:

$$e^{j(\theta_p - \theta_q)} = e^{j\Delta\theta} = e^{j(2\pi f \tau_{p,q})} \iff \tau_{p,q} = \frac{\Delta\theta}{2\pi f}, \tag{1}$$

where j is the imaginary unit, and θ_p and θ_q denote the phases at channels p and q, respectively. At higher frequencies, phase varies more rapidly, enabling finer resolution of the TDOA. However, since phase is wrapped within $[-\pi, \pi)$, the same IPD value may correspond to multiple TDOAs, resulting in spatial aliasing, as illustrated in Fig. 1(b). The aliasing condition depends on the microphone spacing r and the maximum unambiguous frequency $f_{\max}$:

$$f \leq f_{\max} = \frac{v}{2r} \iff r \leq \frac{\lambda}{2}, \quad \lambda = \frac{v}{f}, \tag{2}$$

where v is the speed of sound and λ is the wavelength corresponding to f. Thus, aliasing can be avoided either by reducing the microphone spacing r below half the wavelength of f_{max} or by limiting the frequency below f_{max}. In summary, lower frequencies are alias-free but provide coarse TDOA resolution, while higher frequencies yield finer resolution at the cost of potential aliasing. As MA geometries vary widely across real-world applications, accounting for this trade-off is crucial for geometry-invariant SSL.

2.2 Output Representation Paradigms in DNN-based SSL

The outputs of DNN-based SSL can be broadly categorized into regression and classification approaches. Regression methods directly predict source locations in 3D coordinates (Diaz-Guerra et al., 2021a; Grinstein et al., 2024). They offer theoretically infinite resolution, but suffer from limited interpretability, since they predict only coordinates rather than a spatial spectrum indicating source likelihood across the entire space. Furthermore, their architectures are typically constrained by the maximum number of sources. Classification-based methods discretize the 3D space into predefined DOA grids (Schwartz et al., 2023; Baek et al., 2025). This yields interpretable spatial spectra without being tied to the number of sources, but performance is bounded by grid resolution, and retraining is required when adopting new grids. To balance these trade-offs, template matching (Yang et al., 2021; Wang et al., 2024b) has been explored. This approach enables SSL on arbitrary grids without retraining by comparing outputs with IPD templates from candidate DOAs. However, as the model is optimized for IPD estimation rather than direct DOA prediction, performance can degrade. Moreover, template matching requires pairwise outputs for each microphone pair and a predefined number of sources, leading to increased computational cost. These limitations motivate the proposed AGG-RL framework, which enables flexible-grid SSL with direct candidate DOA prediction, without relying on handcrafted templates or pairwise computations.

3 Proposed Framework

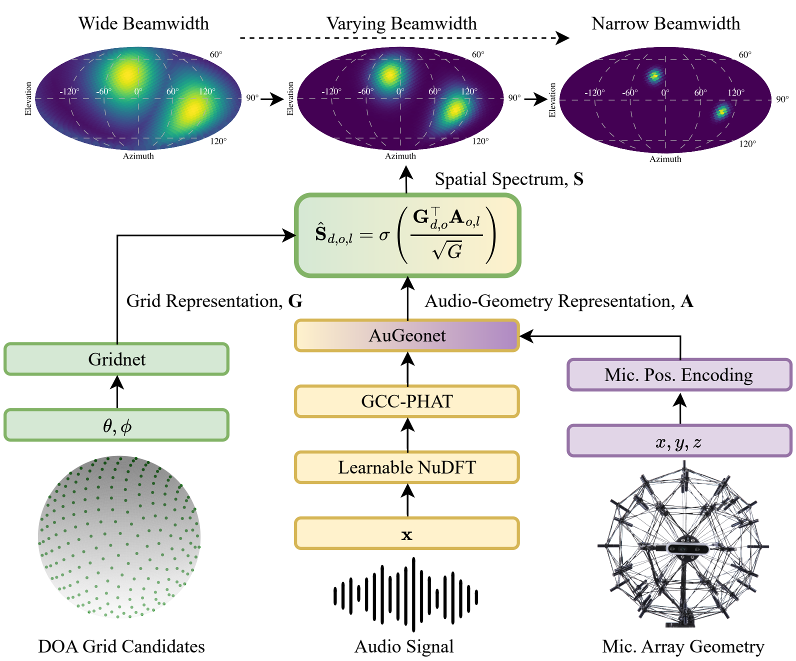

Figure 2: Overview of the proposed framework. The model takes audio signals, microphone array geometries, and candidate DOA grids as inputs, and outputs spatial spectra over the grid. Multiple oracle spatial spectra with different beamwidth parameters are also shown. The microphone array shown (Sphere48 AC Pro by gfai tech GmbH) is reproduced with permission.

To achieve grid-flexible and geometry-invariant SSL, we propose AGG-RL, illustrated in Fig. 2. The framework consists of two networks: the audio-geometry representation network (AuGeonet), $\mathcal{A}(\cdot)$, and the grid representation network (Gridnet), $\mathcal{G}(\cdot)$. AuGeonet integrates two physics-informed components—LNuDFT and rMPE—to extract robust AGRs, while Gridnet produces GRs from candidate DOA grids. AGRs and GRs are projected into a shared latent space, and their similarity is measured by an inner product, where larger values indicate higher likelihood of source presence. The models are trained using soft-labeled oracle spatial spectra (shown at the top of Fig. 2) as supervision, enabling effective learning of audio-geometry-grid relationships.

3.1 Learnable Non-Uniform Discrete Fourier Transform

In contrast to the standard DFT, which uses uniformly spaced frequency bins, the NuDFT (Bagchi & Mitra, 1996a;b; 1999) employs non-uniform frequency bin allocations that can be optimal for specific applications (Wei & Yang, 2022; Wen & Houlihan, 2023; de Haan et al., 2002; Chang, 2005; Muralishankar et al., 2020; Lim et al., 2024). While NuDFT can also be defined with non-uniform sampling along the time axis, here we focus on non-uniformity along the frequency axis. In SSL, NuDFT enables more effective extraction of IPD features by emphasizing physically informative frequency ranges with densely sampled bins, discussed in Section 2.1.

Let $\mathbf{x}_c \in \mathbb{R}^T$ denote the T-sample signal received at the c-th channel of a C-channel MA, which is a mixture of multiple speakers, noise, and reverberation. The frequency-domain representation $\mathbf{X}_c$ is obtained by applying the LNuDFT independently to each channel, defined as:

$$\mathbf{X}_c[k,l] = \sum_{n=0}^{N-1} \underbrace{\mathbf{x}_c[n+N_l]\; w[n]}_{\text{windowed frame}} \cdot \underbrace{e^{-j2\pi \frac{n}{N}\nu_k}}_{\text{LNuDFT basis}}, \tag{3}$$

where c denotes the channel index, $k \in \{0, \ldots, K-1\}$ the frequency-bin index, and l the frame index. N is the frame length, N_l the starting sample of the l-th frame, and $w[\cdot]$ is a window function. ν_k denotes the location of the k-th frequency bin, which maps to the physical frequency $f_k = \frac{\nu_k}{N} f_s$ with sampling frequency f_s. When $K = \frac{N}{2} + 1$ and $\nu_k = k$, Eq. (3) reduces to the standard DFT. For the proposed LNuDFT, ν_k are treated as learnable parameters instead of being fixed as in the NuDFT, enabling the model to allocate frequency bins more densely in regions that convey physically informative phase cues for SSL. To ensure monotonic ordering and compliance with the Nyquist limit ($0 \le \nu_0 < \ldots < \nu_{K-1} \le \frac{N}{2}$, the maximum representable frequency), ν_k is defined as the cumulative sum of positive, learnable increments a_k between adjacent bins:

$$\nu_0 = 0, \quad \nu_k = \nu_{k-1} + a_{k-1}, \quad a_k > 0 \;\; \forall k \in \{1, 2, \ldots, K-1\}. \tag{4}$$

To ensure effective initialization, ν_k^{init} and a_k^{init} are assigned using a logit-based mapping that allocates bins more densely in the mid-frequency range, as follows:

$$\tilde{\nu}_k = \epsilon_{\text{start}} + \frac{\epsilon_{\text{end}} - \epsilon_{\text{start}}}{K-1}\, k \;\; \in (\epsilon_{\text{start}}, \epsilon_{\text{end}}), \quad \hat{\nu}_k = \ln\left(\frac{\tilde{\nu}_k}{1-\tilde{\nu}_k}\right), \tag{5}$$

$$\nu_k^{\text{init}} = \frac{\hat{\nu}_k - \nu_0}{\hat{\nu}_{K-1}} \cdot (K-1), \quad a_{k-1}^{\text{init}} = \nu_k^{\text{init}} - \nu_{k-1}^{\text{init}}, \tag{6}$$

where $0 < \epsilon_{\text{start}} < \epsilon_{\text{end}} < 1$ are hyperparameters that prevent saturation of the logit function. After each gradient update, the following constraints are applied to preserve monotonicity and the Nyquist limit:

$$\hat{a}_k = \min\left(\max\left(\tilde{a}_k, \epsilon_{\min}\right), \epsilon_{\max}\right), \tag{7}$$

$$a_k = \begin{cases} \dfrac{\hat{a}_k}{\sum_{\hat{k}=0}^{K-1} \hat{a}_{\hat{k}}} \cdot \dfrac{N}{2}, & \text{if } \sum_{\hat{k}=0}^{K-1} \hat{a}_{\hat{k}} > \frac{N}{2}, \\ \hat{a}_k, & \text{otherwise}, \end{cases} \tag{8}$$

where $\tilde{a}_k$ is the raw parameter updated by gradient descent, clipped to $(\epsilon_{\min}, \epsilon_{\max})$ to enforce positivity and avoid extreme values. Normalization in Eq. (8) guarantees that ν_k is bounded by $\frac{N}{2}$. An illustration of LNuDFT is provided in Appendix A.2. Additionally, LNuDFT can be efficiently implemented as 1D convolution (Bagchi & Mitra, 1996a;b), where basis functions serve as convolution kernels of size N and feature dimension K, with hop size H. This adaptive allocation of frequency bins during training preserves phase information while enhancing robustness and interpretability by focusing on physically informative frequency regions relevant to IPD.

3.2 Relative Phase Feature and Microphone Positional Encoding

As MA geometries vary widely across applications, numerous geometry-invariant methods have been explored (Luo et al., 2020; Pandey et al., 2022; Yoshioka et al., 2022; Mu et al., 2024; Xu et al., 2025). In parallel, several geometry-aware approaches have been proposed for SSL (Grinstein et al., 2024; Schwartz et al., 2023; Wang et al., 2024b; Baek et al., 2025). Recognizing that TDOA patterns inherently depend on the MA geometries, GI-DOAEnet (Baek et al., 2025) stands as a representative example, explicitly incorporating geometry information via aMPE and channel-wise multi-head self-attention (CW-MHSA) (Vaswani et al., 2017; Pandey et al., 2022). Here, CW-MHSA computes pairwise channel similarities, while aMPE injects geometry information as positional encodings. This design illustrates how geometry-aware features can be directly embedded into the network to enhance robustness across different MA configurations. Building on this framework, we present AuGeonet, a modified version of GI-DOAEnet that integrates LNuDFT-based GCC-PHAT features and rMPEs, aiming to improve generalization to unseen MA configurations.

Relative phase features. To better exploit IPDs, instead of raw DFT coefficients, we adopt GCC-PHAT (Knapp & Carter, 1976) in frequency-domain that emphasizes phase differences while suppressing magnitude variations. Computing all pairwise GCC-PHAT features scales as $\mathcal{O}(C^2)$, so we employ a reference-based scheme that reduces complexity to $\mathcal{O}(C)$. The reference channel $\bar{c}$ is chosen as the microphone closest to the MA center, and the LNuDFT-based GCC-PHAT is defined:

$$\hat{\mathbf{X}}_c^{\text{GCC}}[k,l] = \frac{\mathbf{X}_c[k,l]\ \mathbf{X}_{\bar{c}}^*[k,l]}{|\mathbf{X}_c[k,l]|\ |\mathbf{X}_{\bar{c}}[k,l]|}, \tag{9}$$

where * denotes complex conjugation and $|\cdot|$ the magnitude. The resulting feature $\hat{\mathbf{X}}^{\text{GCC}} \in \mathbb{C}^{(C-1)\times K\times L}$ is split into real and imaginary parts and concatenated along the frequency axis, producing $\mathbf{X}^{\text{GCC}} \in \mathbb{R}^{(C-1)\times 2K\times L}$. This emphasizes relative phase cues while reducing input dimensionality to $C-1$ by excluding the reference channel.

Relative microphone positional encoding. Inspired by the inherently relative nature of IPDs and relative positional encodings (Shaw et al., 2018; Pham et al., 2020; Su et al., 2024), we introduce rMPE, which encodes each microphone's coordinates relative to a reference channel. This design directly aligns with the physics of sound propagation, where TDOA and IPD depend solely on relative microphone positions (see Appendix A.1). Let $\mathbf{p}_c = (x_c, y_c, z_c)$ denote the Cartesian coordinates of microphone c. The relative coordinates are:

$$\begin{gathered} \tilde{x}_c = x_c - x_{\bar{c}}, \quad \tilde{y}_c = y_c - y_{\bar{c}}, \quad \tilde{z}_c = z_c - z_{\bar{c}}, \\ \tilde{r}_c = \sqrt{\tilde{x}_c^2 + \tilde{y}_c^2 + \tilde{z}_c^2}, \quad \tilde{\vartheta}_c = \operatorname{atan2}(\tilde{y}_c, \tilde{x}_c), \quad \tilde{\varphi}_c = \tfrac{\pi}{2} - \operatorname{atan2}(\tilde{z}_c, \sqrt{\tilde{x}_c^2 + \tilde{y}_c^2}) \end{gathered} \tag{10}$$

where $\tilde{r}_c \in [0,\infty)$, $\tilde{\vartheta}_c \in [-\pi,\pi)$, and $\tilde{\varphi}_c \in [0,\pi]$ represent the distance, azimuth, and elevation, respectively. Following aMPE, rMPE encodes these spherical coordinates into sinusoidal encodings:

$$\mathbf{v}(Q) = \tfrac{4}{Q}\left[0, 1, \ldots, \tfrac{Q}{4} - 1\right]^\top \in \mathbb{R}^{\frac{Q}{4}}, \tag{11}$$

$$\begin{aligned} \mathcal{P}_c^{\text{PM}} &= h_{\text{PM}}(\tilde{r}_c, \tilde{\vartheta}_c, \tilde{\varphi}_c; \alpha, \beta, M) & \mathcal{P}_c^{\text{FM}} &= h_{\text{FM}}(\tilde{r}_c, \tilde{\vartheta}_c, \tilde{\varphi}_c; \alpha, \beta, M) \\ &= \alpha\tilde{r}_c \begin{bmatrix} \cos(2\pi\beta\,\mathbf{v}(M) + \tilde{\vartheta}_c) \\ \sin(2\pi\beta\,\mathbf{v}(M) + \tilde{\vartheta}_c) \\ \cos(2\pi\beta\,\mathbf{v}(M) + \tilde{\varphi}_c) \\ \sin(2\pi\beta\,\mathbf{v}(M) + \tilde{\varphi}_c) \end{bmatrix}, & &= \alpha\tilde{r}_c \begin{bmatrix} \cos(\tilde{\vartheta}_c\,\beta\,\mathbf{v}(M)) \\ \sin(\tilde{\vartheta}_c\,\beta\,\mathbf{v}(M)) \\ \cos(\tilde{\varphi}_c\,\beta\,\mathbf{v}(M)) \\ \sin(\tilde{\varphi}_c\,\beta\,\mathbf{v}(M)) \end{bmatrix}, \end{aligned} \tag{12}$$

where $\mathbf{v}(Q)$ uniformly partitions the range $[0,1)$ into $\frac{Q}{4}$ elements, and $^\top$ is a transpose operation. $h_{\text{PM}}(\cdot)$ and $h_{\text{FM}}(\cdot)$ denote the phase-modulated (PM) and frequency-modulated (FM) rMPE mapping functions, respectively. α is a scaling factor, β a frequency factor, and M the target feature dimension. Stacking across all non-reference microphones yields $\mathcal{P} \in \mathbb{R}^{(C-1)\times M}$, aligned with the input features and CW-MHSA to provide positional cues. With the proposed LNuDFT-based GCC-PHAT and rMPE integrated into AuGeonet, we obtain AGRs, $\mathbf{A}$:

$$\mathbf{A} = \mathcal{A}(\mathbf{x}, \mathbf{p}; \boldsymbol{\Theta}) \in \mathbb{R}^{O\times G\times L}, \tag{13}$$

where G is the AGR dimensionality, O is the number of outputs in the deeply supervised curriculum learning (DSCL) framework (Baek et al., 2023), and $\boldsymbol{\Theta}$ denotes the learnable parameters of

AuGeonet. The architectural details of AuGeonet are provided in Appendix A.3. These AGRs naturally capture audio-geometry relationships and are later integrated into AGG-RL to estimate spatial spectra over candidate DOAs.

3.3 Audio-Geometry-Grid Representation Learning

To overcome the limitations of fixed-grid classification, discussed in Section 2.2, we propose AGG-RL, which aligns AGRs with GRs and produces a probabilistic spatial spectrum over arbitrary candidate DOAs by measuring their similarity. We first encode the d-th candidate DOA, with azimuth angle θ_d and elevation angle ϕ_d, into a G-dimensional sinusoidal vector, analogous to Eq. (12) of PM-based rMPE:

$$\hat{\mathbf{G}}_d = h_{\mathrm{Grid}}(\theta_d, \phi_d; \xi, G) = \begin{bmatrix} \cos(2\pi\xi\, \mathbf{v}(G) + \theta_d) \\ \sin(2\pi\xi\, \mathbf{v}(G) + \theta_d) \\ \cos(2\pi\xi\, \mathbf{v}(G) + \phi_d) \\ \sin(2\pi\xi\, \mathbf{v}(G) + \phi_d) \end{bmatrix} \in \mathbb{R}^G, \tag{14}$$

where $h_{\mathrm{Grid}}(\cdot)$ denotes the grid encoding function, and ξ is a modulation frequency. Using Gridnet $\mathcal{G}_o(\cdot)$, a simple DNN with learnable parameters $\mathbf{\Psi}_o$ specific to each output index o (see Appendix A.4), $\hat{\mathbf{G}}_d$ is transformed into a GR:

$$\mathbf{G}_{d,o} = \mathcal{G}_o\left(\hat{\mathbf{G}}_d; \mathbf{\Psi}_o\right) \in \mathbb{R}^G. \tag{15}$$

Given AGRs $\mathbf{A} \in \mathbb{R}^{O \times G \times L}$ from AuGeonet, the similarity is computed by a scaled inner product followed by a sigmoid function $\sigma(\cdot)$, producing the probabilistic spatial spectrum:

$$\hat{\mathbf{S}}_{d,o,l} \;=\; \sigma\left(\frac{\mathbf{G}_{d,o}^{\top}\mathbf{A}_{o,l}}{\sqrt{G}}\right) \in [0, 1], \tag{16}$$

where scaling by $\sqrt{G}$ stabilizes optimization by controlling the variance of the inner product (Vaswani et al., 2017). Through this procedure, AGRs are encouraged to align with GRs at true-source DOAs while diverging from non-source directions. Meanwhile, GRs are trained to represent candidate DOAs independently of the audios and MA geometries, enabling flexible-grid SSL.

Candidate DOAs are sampled using Fibonacci sphere points (Saff & Kuijlaars, 1997), providing near-uniform coverage over the unit sphere. During training, Fibonacci grids with D points are randomly rotated for data augmentation. Soft targets are defined as oracle spatial spectra with varying beamwidths (Baek et al., 2023) and used in a weighted binary cross-entropy (BCE) loss (Nguyen et al., 2020), which emphasizes positive samples. At inference, an iterative peak detection algorithm (Baek et al., 2023) is applied to the final layer output to identify multiple source DOAs. Further details are given in Appendix A.5–A.8. In summary, AGG-RL enables flexible-grid and geometry-invariant SSL without retraining, while retaining the interpretability of classification-based methods.

4 Experimental Setup

4.1 Model Implementation and Baselines

We compared our method against classical baselines (MUSIC (Schmidt, 1986), SRP-PHAT (Dibiase, 2000)) and recent DNN-based methods (Unet (Schwartz et al., 2023), Neural-SRP (Grinstein et al., 2024), GI-DOAEnet (Baek et al., 2025)). To ensure fair comparison, all methods were implemented in a causal setting with identical DFT parameters ($N = 512$, $K = 257$, $H = 128$) and a Hanning window. For classical methods, candidate DOAs were sampled using Fibonacci grids with $D = 512$ and 2048. Unet and Neural-SRP were modified following GI-DOAEnet to produce multiple spatial spectra outputs, following Baek et al. (2025). Unet was re-implemented from the original paper, while Neural-SRP[1] and GI-DOAEnet[2] were adapted from public code. Unet used SRP-PHAT input with $D = 512$, whereas Neural-SRP employed time-domain GCC-PHAT features; both were

[1] `https://github.com/egrinstein/neural_srp`
[2] `https://github.com/BaekMS/GI-DOAEnet`

adapted to output spectra on a Fibonacci grid with $D = 2048$. For GI-DOAEnet, both PM- and FM-based aMPE variants were evaluated, with an output dimension of $D = 2048$. We additionally note that IPDnet with template matching (Wang et al., 2024b) was excluded from direct comparison due to its impractical computational cost (23.2 GFLOPs for 2-channel input, making it prohibitive for larger MAs) and incompatible output format (estimates microphone pairwise, frequency-dependent IPDs instead of DOAs). For the proposed method, FM-based rMPE was adopted as default, as it slightly outperformed PM-based encoding in preliminary experiments, and $D = 2048$ was used for consistency. For LNuDFT of AuGeonet, initialization was performed with $\epsilon_{\text{start}} = 0.15$ and $\epsilon_{\text{end}} = 0.95$, and constraints were applied with $\epsilon_{\min} = 0.01$ and $\epsilon_{\max} = 100$. All DNN-based methods followed the same training setup described in Appendix A.9.

4.2 Dataset and Evaluation Metrics

Table 1: Parameters used for synthetic dataset generation.

Parameter	Interval	Unit
Number of speakers	[1, 2]	-
RT60	[0.2, 1.3]	s
Room size	[3×3×2.5, 10×8×6]	m^3
Distance	[0.3, 2.5]	m
Azimuth	[0, 360)	°
Elevation	[0, 180]	°
SNR (speech vs. noise)	[-5, 30]	dB
SIR (between speakers)	[-5, 5]	dB
SIR (between noises)	[-15, 15]	dB

Synthetic datasets were used for training, validation, and partial evaluation. The training set was generated on-the-fly to provide diverse conditions, with a fixed number of channels per batch. Table 1 summarizes the ranges of acoustic and spatial parameters used to generate the synthetic mixtures, including reverberation time (RT60), signal-to-noise ratio (SNR) between speech and noise, and signal-to-interference ratio (SIR) between speakers or between noise sources. For each sample, we simulated multi-channel room impulse responses (RIRs) using the image source method (Allen & Berkley, 1979) implemented in gpuRIR (Diaz-Guerra et al., 2021b). Speech signals were drawn from LibriSpeech (Panayotov et al., 2015) and noise signals from MS-SNSD (Reddy et al., 2019), each cropped to 4 seconds. Additional implementation details for the synthetic data generation are provided in Appendix A.10.

Table 2: Evaluation dataset configuration.

Dataset	Real Dataset	Microphone Array	Channels	Training Exposure
NAO robot	✓	NAO robot	12	✓ (seen)
Eigenmike	✓	Eigenmike	32	✗ (unseen)
Dynamic-S	✗	Dynamic	4–12	✓ (seen)
Dynamic-U	✗	Dynamic	13–16	✗ (unseen)

After training, the model with the lowest validation loss was selected for evaluation. Evaluation was conducted using four datasets, as shown in Table 2. Real recordings were taken from LOCATA (Löllmann et al., 2018), where *NAO robot* and *Eigenmike* datasets consisted of recordings using the NAO robot[3] and the Eigenmike[4], respectively. Only non-moving sources with up to two speakers were used for evaluation, resampled to 16 kHz. Two synthetic datasets, *Dynamic-S* and *Dynamic-U*, were constructed to evaluate generalization to seen and unseen numbers of channels, respectively, across a variety of MA geometries. These synthetic datasets were generated with 300 utterances per channel, following the same procedure as the training set but using different source material: TIMIT (Garofolo et al., 1993) for speech and ESC-50 (Piczak, 2015) for noise. For evaluation metrics, we used mean absolute error (MAE, °) and accuracy (ACC_{10}, %) (see Appendix A.11). MAE measured the average angular error; lower values indicate better performance. ACC_{10} measured the percentage

[3] https://www.aldebaran.com/en/nao
[4] https://eigenmike.com/eigenmike-em32

of predictions within a 10° margin; higher values indicate better performance. Both metrics were computed per utterance and averaged over each set.

5 RESULTS AND DISCUSSION

Table 3: Experimental results with different methods. The best results on each dataset are in **bold**.

	NAO robot		*Eigenmike*		*Dynamic-S*		*Dynamic-U*	
	MAE	ACC_{10}	MAE	ACC_{10}	MAE	ACC_{10}	MAE	ACC_{10}
$MUSIC_{512}$	20.63 ± 2.44	64.95	29.93 ± 3.09	36.37	30.35 ± 0.63	27.94	27.13 ± 0.89	33.20
$MUSIC_{2048}$	19.31 ± 2.65	69.77	29.78 ± 3.06	36.68	30.24 ± 0.63	28.50	26.88 ± 0.90	33.92
$SRP\text{-}PHAT_{512}$	22.36 ± 1.79	67.95	27.45 ± 1.73	41.38	43.98 ± 0.70	24.55	38.64 ± 1.03	32.13
$SRP\text{-}PHAT_{2048}$	21.77 ± 1.73	67.84	26.88 ± 1.93	53.22	43.89 ± 0.70	25.10	38.40 ± 1.04	32.39
Unet	10.89 ± 1.53	86.25	14.89 ± 1.76	65.82	19.94 ± 0.69	58.88	19.15 ± 0.94	60.57
with AGG-RL	12.79 ± 3.26	77.33	16.86 ± 3.26	55.69	21.23 ± 0.69	53.74	20.11 ± 0.95	56.08
Neural-SRP	9.72 ± 2.28	78.66	52.75 ± 18.61	22.16	19.60 ± 0.74	52.32	21.18 ± 1.01	45.51
with AGG-RL	9.89 ± 2.55	72.80	13.25 ± 2.32	37.07	19.79 ± 0.74	50.56	19.05 ± 1.01	54.13
GI-DOAEnet$^{\mathrm{FM}}$	11.31 ± 2.54	77.36	93.61 ± 13.06	0.00	15.49 ± 0.55	64.36	54.81 ± 1.73	6.10
GI-DOAEnet$^{\mathrm{PM}}$	12.26 ± 2.27	72.47	77.09 ± 13.32	2.82	17.40 ± 0.59	58.54	79.17 ± 1.81	0.58
Proposed	**8.25** ± 1.52	**90.78**	**11.24** ± 1.76	**72.17**	10.32 ± 0.49	77.34	14.12 ± 0.77	63.17
(i) rMPE-PM	8.38 ± 1.63	89.85	13.42 ± 2.00	70.09	11.55 ± 0.50	74.46	12.46 ± 0.78	67.97
(ii) DFT	13.24 ± 2.97	72.32	111.21 ± 9.86	0.00	16.47 ± 0.58	60.83	87.71 ± 1.89	0.92
(iii) DFT + GCC-PHAT	9.17 ± 3.44	87.74	16.53 ± 3.97	39.35	10.26 ± 0.48	77.56	17.90 ± 0.71	45.11
(iv) LNuDFT + Uniform init.	8.69 ± 2.97	90.03	15.13 ± 2.68	40.70	10.44 ± 0.47	77.69	23.03 ± 0.89	36.05
(v) NuDFT + Logit init.	8.96 ± 2.83	89.34	17.34 ± 2.47	28.52	10.64 ± 0.48	76.56	**11.83** ± 0.66	**72.77**
(vi) Fixed grid	9.17 ± 2.28	87.31	13.58 ± 2.60	40.82	**9.57** ± 0.46	**81.70**	13.84 ± 1.07	65.29
(vii) Gridnet with FM Enc.	9.95 ± 2.36	85.60	12.58 ± 2.68	50.55	11.10 ± 0.49	75.49	15.24 ± 0.68	58.60
(viii) Gridnet with Cartesian	9.08 ± 2.85	88.17	11.87 ± 2.80	64.62	10.41 ± 0.48	77.28	23.10 ± 0.91	34.26

Table 3 presents the overall results on the evaluation datasets. Rows above the double line correspond to baseline methods, while rows below represent the proposed method and its ablation studies. The 95% confidence intervals (CIs) for the MAE are reported using $\pm$ values, which indicate the corresponding margin of error.

Comparison with baselines. The subscripts 512 and 2048 indicate the number of grids used for SRP-PHAT and MUSIC. Both methods consistently underperformed compared to DNN-based approaches across all datasets. Moreover, increasing the number of grid points did not lead to meaningful improvements. Accordingly, Unet adopted SRP-PHAT with $D = 512$ for efficiency. Among the DNN-based baselines, Neural-SRP achieved lower MAE than Unet on the *NAO robot* and *Dynamic-S* datasets, while Unet outperformed Neural-SRP on the remaining datasets and metrics. Notably, Neural-SRP exhibited substantial performance degradation on *Eigenmike*. When AGG-RL was applied, performance of Unet slightly degraded overall. In contrast, Neural-SRP showed performance drops in seen conditions such as *NAO robot* and *Dynamic-S*, but significant improvements under unseen conditions, including *Eigenmike* and *Dynamic-U*. These results demonstrate that AGG-RL effectively enhanced generalizability for Neural-SRP. GI-DOAEnet variants with different aMPE types outperformed Unet and Neural-SRP on *Dynamic-S*, which shared the same channel configuration as the training set. However, their performance dropped significantly under unseen settings, including *Eigenmike* and *Dynamic-U*.

The proposed method consistently achieved superior performance across all datasets, clearly validating its robustness and effectiveness. However, it achieved slightly worse results on unseen conditions compared to the seen conditions. It indicates a performance gap between seen and unseen scenarios but still outperformed all baselines. To further validate these findings, we provide box and violin plots (Appendix A.12) to examine the distribution of errors, results under different acoustic conditions (Appendix A.13) to assess robustness across diverse environments, and spatial spectrum visualizations (Appendix A.15) to illustrate the interpretability and stability of the proposed method. Additionally, Appendix A.14 reports results on the STARSS23 dataset (Shimada et al., 2023), further demonstrating the effectiveness of the method on a real-world benchmark with different recording conditions. The following ablation studies further clarify the contributions of each component.

Effectiveness of GCC-PHAT and rMPE. Experiment (i) replaced rMPE with PM-based one. This variant showed comparable but slightly inferior performance on most datasets, except for *Dynamic-U*, indicating that FM was more effective than PM for rMPE. Accordingly, all proposed and subsequent ablation studies adopted FM-based rMPE as the default. In experiment (ii), both GCC-PHAT and rMPE were replaced with the standard DFT and FM-based aMPE, respectively. This led to a consistent performance drop across all datasets, underscoring the importance of relative representations introduced by GCC-PHAT and rMPE. In both GI-DOAEnet and AuGeonet, CW-MHSA layers were used to capture channel-wise relationships. However, prior works (Kazemnejad et al., 2023; Zhou et al., 2024) have shown that MHSA performance degrades when extrapolating to longer sequences than those encountered during training. We therefore hypothesize that the relative nature of GCC-PHAT and rMPE mitigated this limitation, thereby enhancing generalization to unseen conditions.

Effectiveness of LNuDFT. Experiments (iii)–(v) evaluated the contribution of LNuDFT under different configurations. In experiment (iii), LNuDFT was replaced with the standard DFT while retaining GCC-PHAT and rMPE. Performance degraded on all datasets except *Dynamic-S*, validating the effectiveness of LNuDFT. Experiment (iv) initialized LNuDFT with the uniform spacing, identical to the standard DFT and allowed it to be trained. While it achieved comparable results to the proposed method on *Dynamic-S* and *NAO robot*, performance decreased on *Eigenmike* and *Dynamic-U*. In experiment (v), NuDFT parameters were initialized using a proposed logit-based mapping and then frozen during training. This variant yielded the best performance on *Dynamic-U*, suggesting that initializing LNuDFT with a informative frequency distribution benefitted generalization to unseen conditions. While logit-based initialization was more effective in practice, the choice of mapping function and hyperparameters was made empirically. Identifying optimal initialization strategies remains an open direction for future research and may further enhance performance. The visualization of trained LNuDFT parameters (Appendix A.2) reveals that they densely focused on physically informative frequency regions, enhancing both model interpretability and robustness.

Effectiveness of AGG-RL. In experiment (vi), AGG-RL was replaced with a fixed-grid setup ($D = 2048$), directly predicting spatial spectra as in standard classification models. This variant achieved the best performance on *Dynamic-S*, which matched the training condition, and slightly outperformed the proposed method on *Dynamic-U*. However, it degraded on real datasets, showing that AGG-RL was crucial for generalization. Experiments (vii) and (viii) replaced Gridnet inputs with FM-based encodings of Eq. (12) and raw Cartesian coordinates, respectively. FM-based encoding achieved similar results, but PM-based encoding was slightly superior overall. Raw Cartesian inputs yielded comparable performance on most datasets but dropped on *Dynamic-U*, suggesting that sinusoidal encodings better captured the candidate DOA grid structure.

Table 4: Experimental results with different numbers of candidate grids D. The best results on each dataset are in **bold**.

D	*NAO robot*		*Eigenmike*		*Dynamic-S*		*Dynamic-U*	
	MAE	ACC_{10}	MAE	ACC_{10}	MAE	ACC_{10}	MAE	ACC_{10}
128	12.69 ± 3.14	68.01	13.60 ± 2.83	58.65	13.84 ± 0.45	60.29	16.34 ± 0.72	45.70
256	10.92 ± 2.79	81.25	13.51 ± 3.15	58.20	13.11 ± 0.51	69.79	16.32 ± 0.80	51.33
512	10.19 ± 2.17	87.51	11.65 ± 2.72	61.06	11.59 ± 0.49	74.60	14.97 ± 0.77	61.27
1024	9.21 ± 2.65	89.91	12.13 ± 2.86	72.66	10.66 ± 0.49	77.52	14.24 ± 0.76	61.88
2048	**8.25** ± 1.52	**90.78**	**11.24** ± 1.76	72.17	10.32 ± 0.49	77.34	14.12 ± 0.77	63.17
4096	9.16 ± 2.56	89.91	11.51 ± 2.68	73.06	10.14 ± 0.50	77.73	14.01 ± 0.77	63.72
8192	8.91 ± 2.63	89.54	11.52 ± 2.76	**75.97**	**9.91** ± 0.49	78.12	**13.85** ± 0.76	63.83
16384	8.79 ± 2.63	89.04	11.54 ± 2.80	72.48	9.96 ± 0.50	**78.21**	13.87 ± 0.77	**64.18**

Table 4 further reports the results of the proposed method with varying D. When D was too small, performance dropped due to limited spatial resolution. Once $D \geq 512$, performance stabilized across all datasets, confirming the grid-flexibility of AGG-RL. When D exceeded 2048, the trends between the real and synthetic datasets diverged slightly. For the synthetic datasets (*Dynamic-S* and *Dynamic-U*), the performance continued to improve mildly with larger D. Since these datasets were closely matched to the simulated training domain, finer angular discretization reduced quantization error and provided consistent, though marginal, improvements. This indicates diminishing returns beyond a certain resolution. In contrast, performance on the real datasets (*NAO robot* and *Eigenmike*) showed a slight degradation once D exceeded 2048 (except for ACC_{10} on *Eigenmike*). Real-world recordings inevitably contained small acoustic mismatches—such as sensor noise, microphone manufacturing tolerances, and RIR deviations—that were not present in synthetic data. With an overly dense grid, the localization decision became more sensitive to these perturbations, increasing estimation variance. Overall, the results suggest that increasing D beyond a certain threshold yields limited gains, and excessively large D is not necessarily beneficial in practice. t-SNE visualizations of the GRs (Appendix A.16) further confirm that Gridnet learned structured spatial embeddings. Overall, AGG-RL enhanced robustness on real recordings and unseen conditions, effectively integrating audio-geometry-grid information into a shared latent space.

Table 5: Number of parameters and FLOPs under different configurations.

(a) Models with varying number of channels

Model	Params (M)	FLOPs (G)		
		$C=4$	$C=8$	$C=12$
Unet	8.40	1.14	1.49	2.10
Neural-SRP	1.13	1.86	8.54	20.08
GI-DOAEnet	2.32	0.49	0.89	1.29
AuGeonet				
with Fixed Grid	2.32	0.42	0.82	1.22
with AGG-RL	1.86	0.43	0.83	1.23

(b) Gridnet with varying grid sizes

D	Gridnet Params (M)	GR Params (M)	FLOPs (G)
1024	1.19	0.26	0.27
2048	1.19	0.52	0.54
4096	1.19	1.04	1.07

Computational resource comparison. We measured inference complexity using fvcore[5], with 1-second inputs, defaulting to $G = 256$ and $D = 2048$. Table 5(a) compares parameters and FLOPs across different numbers of channels, while Table 5(b) reports Gridnet results with varying grid sizes. Unet had the largest parameter count and Neural-SRP the highest FLOPs, with FLOPs of both models being scaled quadratically with C due to pairwise features. GI-DOAEnet and AuGeonet with fixed grid shared the same parameters, but AuGeonet achieved lower FLOPs with reference-based GCC-PHAT, also ensuring linear scaling in C. With AGG-RL, AuGeonet further reduced parameters by replacing direct $D = 2048$ mapping with a $G = 256$ representation; FLOPs increased only slightly from the similarity computation in Eq. (16). For Gridnet with GRs, FLOPs scaled linearly with D, and both FLOPs and parameter counts were on the same order as AuGeonet, contributing to the overall computational complexity. Nevertheless, FLOPs remained lower than those of baselines and IPDnet (Wang et al., 2024b). In practice, the overhead from Gridnet is manageable: GRs can be cached for static environments, or D can be reduced with minimal performance loss. A more study on efficiency improvements, including lightweight design alternatives, is left for future work.

6 Conclusion

In this paper, we proposed AGG-RL, a novel framework for grid-flexible and geometry-invariant SSL that jointly learns complementary representations from audio-geometry-grid inputs. To improve generalization and interpretability, we introduced two physics-informed components: LNuDFT, which enables adaptive frequency analysis to enhance IPD distinguishability, and rMPE, which encodes relative microphone position cues. Extensive experiments across multiple datasets demonstrated that our framework achieved superior generalizability and robustness, particularly under unseen geometries and real-world recordings. We believe that AGG-RL provides a solid foundation for advancing 3D acoustic scene understanding in practical environments. For future work, we plan to extend AGG-RL to multimodal scenarios and broader spatial sensing tasks that require scalable grid or geometry configurations. We also aim to theoretically analyze the generalization properties of LNuDFT-based representations, providing a stronger foundation for physics-informed DNN.

Reproducibility Statement

In this paper, we leverage publicly available datasets and toolkits to ensure the reproducibility of our experiments. The specific datasets, libraries, and detailed implementation steps are provided in the Appendix. The source code for our work is available at `https://anonymous.4open.science/r/Audio-Geometry-Grid_Representation-Learning-6FD6`.

References

Jont B Allen and David A Berkley. Image method for efficiently simulating small-room acoustics. *The Journal of the Acoustical Society of America*, 65(4):943–950, 1979.

Jimmy Lei Ba, Jamie Ryan Kiros, and Geoffrey E Hinton. Layer normalization. *arXiv preprint arXiv:1607.06450*, 2016.

[5] `https://github.com/facebookresearch/fvcore`

Min-Sang Baek, Joon-Young Yang, and Joon-Hyuk Chang. Deeply supervised curriculum learning for deep neural network-based sound source localization. In *Proceedings of the Interspeech*, pp. 3744–3748, 2023.

Min-Sang Baek, Joon-Hyuk Chang, and Israel Cohen. DNN-based geometry-invariant DOA estimation with microphone positional encoding and complexity gradual training. *IEEE Transactions on Audio, Speech, and Language Processing*, 33:2360–2376, 2025.

Sonali Bagchi and Sanjit K Mitra. The nonuniform discrete Fourier transform and its applications in filter design. I. 1-D. *IEEE Transactions on Circuits and Systems II: Analog and Digital Signal Processing*, 43(6):422–433, 1996a.

Sonali Bagchi and Sanjit K Mitra. The nonuniform discrete Fourier transform and its applications in filter design. II. 2-D. *IEEE Transactions on Circuits and Systems II: Analog and Digital Signal Processing*, 43(6):434–444, 1996b.

Sonali Bagchi and Sanjit K Mitra. *The Nonuniform Discrete Fourier Transform and Its Applications in Signal Processing*. Academic Publishers, Norwell, MA, USA, 1999.

Shanmukha Srinivas Battula, Hassan Taherian, Ashutosh Pandey, Daniel Wong, Buye Xu, and DeLiang Wang. Robust frame-level speaker localization in reverberant and noisy environments by exploiting phase difference losses. In *Proceedings of the IEEE International Conference on Acoustics, Speech and Signal Processing (ICASSP)*, pp. 1–5, 2025.

Jacob Benesty, Jingdong Chen, and Yiteng Huang. *Microphone Array Signal Processing*. Springer, Germany, 2008.

Yoshua Bengio, Aaron Courville, and Pascal Vincent. Representation learning: A review and new perspectives. *IEEE Transactions on Pattern Analysis and Machine Intelligence*, 35(8):1798–1828, 2013.

Amandine Brunetto, Sascha Hornauer, and Fabien Moutarde. NeRAF: 3D scene infused neural radiance and acoustic fields. In *Proceedings of the International Conference on Representation Learning (ICLR)*, pp. 92876–92899, 2025.

Soumitro Chakrabarty and Emanuël A P Habets. Multi-speaker DOA estimation using deep convolutional networks trained with noise signals. *IEEE Journal of Selected Topics in Signal Processing*, 13(1):8–21, 2019.

Joon-Hyuk Chang. Warped discrete cosine transform-based noisy speech enhancement. *IEEE Transactions on Circuits and Systems II: Express Briefs*, 52(9):535–539, 2005.

Sérgio F. Chevtchenko, Belman Jahir Rodríguez, Rafaella Vale, Abishek Soti, Yeshwanth Bethi, Naqib Ibnul, Alexandre Marcireau, Mostafa Rahimi Azghadi, Andrew Wabnitz, and Saeed Afshar. Drone-based sound source localization: A systematic literature review. *IEEE Access*, 13: 94256–94274, 2025.

Kyunghyun Cho, Bart Van Merriënboer, Caglar Gulcehre, Dzmitry Bahdanau, Fethi Bougares, Holger Schwenk, and Yoshua Bengio. Learning phrase representations using RNN encoder–decoder for statistical machine translation. In *Proceedings of the Conference on Empirical Methods in Natural Language Processing (EMNLP)*, pp. 1724–1734, 2014.

Jeonghwan Choi and Joon-Hyuk Chang. Supervised learning approach for explicit spatial filtering of speech. *IEEE Signal Processing Letters*, 29:1412–1416, 2022.

Djork-Arné Clevert, Thomas Unterthiner, and Sepp Hochreiter. Fast and accurate deep network learning by exponential linear units (ELUs). In *Proceedings of the International Conference on Learning Representations (ICLR)*, 2016.

Stefano Damiano, Federico Miotello, Mirco Pezzoli, Alberto Bernardini, Fabio Antonacci, Augusto Sarti, and Toon van Waterschoot. A zero-shot physics-informed dictionary learning approach for sound field reconstruction. In *Proceedings of the IEEE International Conference on Acoustics, Speech and Signal Processing (ICASSP)*, pp. 1–5, 2025.

Jan Mark de Haan, Nedelko Grbić, Ingvar Claesson, and Sven Nordholm. Design and evaluation of nonuniform DFT filter banks in subband microphone arrays. In *Proceedings of the IEEE International Conference on Acoustics, Speech, and Signal Processing (ICASSP)*, pp. II–1173–II–1176, 2002.

David Diaz-Guerra, Antonio Miguel, and Jose R Beltrán. Robust sound source tracking using SRP-PHAT and 3D convolutional neural networks. *IEEE/ACM Transactions on Audio, Speech, and Language Processing*, 29:300–311, 2021a.

David Diaz-Guerra, Antonio Miguel, and Jose R Beltrán. gpuRIR: A Python library for room impulse response simulation with GPU acceleration. *Multimedia Tools and Applications*, 80(4): 5653–5671, 2021b.

Joseph H Dibiase. A high-accuracy, low-latency technique for talker localization in reverberant environments using microphone arrays. *Ph.D. Thesis, Brown University*, 2000.

Antoni Dimitriadis, Siqi Pan, Vidhyasaharan Sethu, and Beena Ahmed. Spatial HuBERT: Self-supervised spatial speech representation learning for a single talker from multi-channel audio. *arXiv preprint arXiv:2310.10922*, 2023.

Ha Manh Do, Karla Conn Welch, and Weihua Sheng. SoHAM: A sound-based human activity monitoring framework for home service robots. *IEEE Transactions on Automation Science and Engineering*, 19(3):2369–2383, 2022.

Nicholas I Fisher, Toby Lewis, and Brian J J Embleton. *Statistical analysis of spherical data*. Cambridge university press, 1993.

Yury Furletov, Volker Willert, and Jürgen Adamy. Auditory scene understanding for autonomous driving. In *Proceedings of the IEEE Intelligent Vehicles Symposium (IV)*, pp. 697–702, 2021.

Leonardo Gabrielli, Stefano Tomassetti, Carlo Zinato, and Francesco Piazza. End-to-end learning for physics-based acoustic modeling. *IEEE Transactions on Emerging Topics in Computational Intelligence*, 2(2):160–170, 2018.

Chuang Gan, Yiwei Zhang, Jiajun Wu, Boqing Gong, and Joshua B Tenenbaum. Look, listen, and act: Towards audio-visual embodied navigation. In *Proceedings of the IEEE International Conference on Robotics and Automation (ICRA)*, pp. 9701–9707, 2020.

John S Garofolo, Lori F Lamel, William M Fisher, Jonathan G Fiscus, and David S Pallett. DARPA TIMIT acoustic-phonetic continous speech corpus CD-ROM. NIST speech disc 1-1.1. *NASA STI/Recon technical report n*, 93:27403, 1993.

Eric Grinstein, Christopher M Hicks, Toon van Waterschoot, Mike Brookes, and Patrick A Naylor. The Neural-SRP method for universal robust multi-source tracking. *IEEE Open Journal of Signal Processing*, 5:19–28, 2024.

Pierre-Amaury Grumiaux, Srđan Kitić, Laurent Girin, and Alexandre Guérin. A survey of sound source localization with deep learning methods. *The Journal of the Acoustical Society of America*, 152(1):107–151, 2022.

Rishabh Gupta, Jianjun He, Rishabh Ranjan, Woon-Seng Gan, Florian Klein, Christian Schneiderwind, Annika Neidhardt, Karlheinz Brandenburg, and Vesa Välimäki. Augmented/Mixed reality audio for hearables: Sensing, control, and rendering. *IEEE Signal Processing Magazine*, 39(3): 63–89, 2022.

Yuhang He, Niki Trigoni, and Andrew Markham. SoundDet: Polyphonic moving sound event detection and localization from raw waveform. In *Proceedings of the International Conference on Machine Learning (ICML)*, pp. 4160–4170, 2021.

Xiaoyang Huang, Yanjun Wang, Yang Liu, Bingbing Ni, Wenjun Zhang, Jinxian Liu, and Teng Li. AudioEar: Single-view ear reconstruction for personalized spatial audio. In *Proceedings of the AAAI Conference on Artificial Intelligence*, pp. 944–952, 2023.

Sergey Ioffe and Christian Szegedy. Batch normalization: Accelerating deep network training by reducing internal covariate shift. In *Proceedings of the International Conference on Machine Learning (ICML)*, pp. 448–456, 2015.

Mingu Jeon, Jae-Kyung Cho, Hee-Yeun Kim, Byeonggyu Park, Seung-Woo Seo, and Seong-Woo Kim. Non-line-of-sight vehicle localization based on sound. *IEEE Transactions on Intelligent Transportation Systems*, 26(2):2321–2338, 2025.

Xenofon Karakonstantis, Diego Caviedes-Nozal, Antoine Richard, and Efren Fernandez-Grande. Room impulse response reconstruction with physics-informed deep learning. *The Journal of the Acoustical Society of America*, 155(2):1048–1059, 2024.

George Em Karniadakis, Ioannis G Kevrekidis, Lu Lu, Paris Perdikaris, Sifan Wang, and Liu Yang. Physics-informed machine learning. *Nature Reviews Physics*, 3(6):422–440, 2021.

Amirhossein Kazemnejad, Inkit Padhi, Karthikeyan Natesan Ramamurthy, Payel Das, and Siva Reddy. The impact of positional encoding on length generalization in Transformers. In *Proceedings of the Advances in Neural Information Processing Systems (NeurIPS)*, pp. 24892–24928, 2023.

Sungnyun Kim, Sungwoo Cho, Sangmin Bae, Kangwook Jang, and Se-Young Yun. Multi-task corrupted prediction for learning robust audio-visual speech representation. In *Proceedings of the International Conference on Representation Learning (ICLR)*, pp. 65598–65619, 2025.

Diederik P Kingma and Jimmy Ba. Adam: A method for stochastic optimization. In *Proceedings of the International Conference on Learning Representations (ICLR)*, pp. 1–15, 2014.

Charles H Knapp and G Clifford Carter. The generalized correlation method for estimation of time delay. *IEEE Transactions on Acoustics, Speech, and Signal Processing*, 24(4):320–327, 1976.

Masanori Koyama, Kenji Fukumizu, Kohei Hayashi, and Takeru Miyato. Neural Fourier transform: A general approach to equivariant representation learning. In *Proceedings of the International Conference on Learning Representations (ICLR)*, pp. 6728–6759, 2024a.

Shoichi Koyama, Juliano G C Ribeiro, Tomohiko Nakamura, Natsuki Ueno, and Mirco Pezzoli. Physics-informed machine learning for sound field estimation: Fundamentals, state of the art, and challenges. *IEEE Signal Processing Magazine*, 41(6):60–71, 2024b.

Yichong Leng, Zehua Chen, Junliang Guo, Haohe Liu, Jiawei Chen, Xu Tan, Danilo Mandic, Lei He, Xiangyang Li, Tao Qin, sheng zhao, and Tie-Yan Liu. BinauralGrad: A two-stage conditional diffusion probabilistic model for binaural audio synthesis. In *Proceedings of the Advances in Neural Information Processing Systems (NeurIPS)*, pp. 23689–23700, 2022.

Kai Li, Wendi Sang, Chang Zeng, Runxuan Yang, Guo Chen, and Xiaolin Hu. SonicSim: A customizable simulation platform for speech processing in moving sound source scenarios. In *Proceedings of the International Conference on Representation Learning (ICLR)*, pp. 67379–67405, 2025a.

Zixuan Li, Shulin He, and Xueliang Zhang. Robust target speaker direction of arrival estimation. In *Proceedings of the IEEE International Conference on Acoustics, Speech and Signal Processing (ICASSP)*, pp. 1–5, 2025b.

Susan Liang, Dejan Markovic, Israel D Gebru, Steven Krenn, Todd Keebler, Jacob Sandakly, Frank Yu, Samuel Hassel, Chenliang Xu, and Alexander Richard. BinauralFlow: A causal and streamable approach for high-quality binaural speech synthesis with flow matching models. In *Proceedings of the International Conference on Machine Learning (ICML)*, pp. 37281–37298, 2025.

Hyungseob Lim, Jihyun Lee, Byeong Hyeon Kim, Inseon Jang, and Hong-Goo Kang. Perceptual neural audio coding with modified discrete cosine transform. *IEEE Journal of Selected Topics in Signal Processing*, 18(8):1490–1505, 2024.

Ju Lin, Niko Moritz, Yiteng Huang, Ruiming Xie, Ming Sun, Christian Fuegen, and Frank Seide. AGADIR: Towards array-geometry agnostic directional speech recognition. In *Proceedings of the IEEE International Conference on Acoustics, Speech and Signal Processing (ICASSP)*, pp. 11951–11955, 2024.

Andrew Luo, Yilun Du, Michael Tarr, Josh Tenenbaum, Antonio Torralba, and Chuang Gan. Learning neural acoustic fields. In *Proceedings of the Advances in Neural Information Processing Systems (NeurIPS)*, pp. 3165–3177, 2022.

Yi Luo, Zhuo Chen, Nima Mesgarani, and Takuya Yoshioka. End-to-end microphone permutation and number invariant multi-channel speech separation. In *Proceedings of the IEEE International Conference on Acoustics, Speech and Signal Processing (ICASSP)*, pp. 6394–6398, 2020.

Heinrich W Löllmann, Christine Evers, Alexander Schmidt, Heinrich Mellmann, Hendrik Barfuss, Patrick A Naylor, and Walter Kellermann. The LOCATA challenge data corpus for acoustic source localization and tracking. In *Proceedings of the IEEE Sensor Array and Multichannel Signal Processing Workshop (SAM)*, pp. 410–414, 2018.

Ben Mildenhall, Pratul P Srinivasan, Matthew Tancik, Jonathan T Barron, Ravi Ramamoorthi, and Ren Ng. NeRF: Representing scenes as neural radiance fields for view synthesis. *Communications of the ACM*, 65(1):99–106, 2021.

Federico Miotello, Ferdinando Terminiello, Mirco Pezzoli, Alberto Bernardini, Fabio Antonacci, and Augusto Sarti. A physics-informed neural network-based approach for the spatial upsampling of spherical microphone arrays. In *Proceedings of the IEEE International Workshop on Acoustic Signal Enhancement (IWAENC)*, pp. 215–219, 2024.

Bingshen Mu, Pengcheng Guo, Dake Guo, Pan Zhou, Wei Chen, and Lei Xie. Automatic channel selection and spatial feature integration for multi-channel speech recognition across various array topologies. In *Proceedings of the IEEE International Conference on Acoustics, Speech and Signal Processing (ICASSP)*, pp. 11396–11400, 2024.

Rangarao Muralishankar, Debayan Ghosh, and Sanjeev Gurugopinath. A novel modified mel-DCT filter bank structure with application to voice activity detection. *IEEE Signal Processing Letters*, 27:1240–1244, 2020.

Thi Ngoc Tho Nguyen, Woon-Seng Gan, Rishabh Ranjan, and Douglas L Jones. Robust source counting and DOA estimation using spatial pseudo-spectrum and convolutional neural network. *IEEE/ACM Transactions on Audio, Speech, and Language Processing*, 28:2626–2637, 2020.

Tsubasa Ochiai, Shinji Watanabe, Takaaki Hori, and John R Hershey. Multichannel end-to-end speech recognition. In *Proceedings of the International Conference on Machine Learning (ICML)*, pp. 2632–2641, 2017.

Vassil Panayotov, Guoguo Chen, Daniel Povey, and Sanjeev Khudanpur. Librispeech: An ASR corpus based on public domain audio books. In *Proceedings of the IEEE International Conference on Acoustics, Speech and Signal Processing (ICASSP)*, pp. 5206–5210, 2015.

Ashutosh Pandey, Buye Xu, Anurag Kumar, Jacob Donley, Paul Calamia, and DeLiang Wang. TPARN: Triple-path attentive recurrent network for time-domain multichannel speech enhancement. In *Proceedings of the IEEE International Conference on Acoustics, Speech and Signal Processing (ICASSP)*, pp. 6497–6501, 2022.

Ngoc-Quan Pham, Thanh-Le Ha, Tuan-Nam Nguyen, Thai-Son Nguyen, Elizabeth Salesky, Sebastian Stüker, Jan Niehues, and Alex Waibel. Relative positional encoding for speech recognition and direct translation. In *Proceedings of the Interspeech*, pp. 31–35, 2020.

Karol J Piczak. ESC: Dataset for environmental sound classification. In *Proceedings of the ACM International Conference on Multimedia*, pp. 1015–1018, 2015.

Maziar Raissi, Paris Perdikaris, and George E Karniadakis. Physics-informed neural networks: A deep learning framework for solving forward and inverse problems involving nonlinear partial differential equations. *Journal of Computational Physics*, 378:686–707, 2019.

Chinmay Rajguru, Giada Brianza, and Gianluca Memoli. Sound localization in web-based 3D environments. *Scientific Reports*, 12(1):12107, 2022.

Chandan K A Reddy, Ebrahim Beyrami, Jamie Pool, Ross Cutler, Sriram Srinivasan, and Johannes Gehrke. A scalable noisy speech dataset and online subjective test framework. In *Proceedings of the Interspeech*, pp. 1816–1820, 2019.

Juliano G C Ribeiro, Shoichi Koyama, Ryosuke Horiuchi, and Hiroshi Saruwatari. Sound field estimation based on physics-constrained kernel interpolation adapted to environment. *IEEE/ACM Transactions on Audio, Speech, and Language Processing*, 32:4369–4383, 2024.

Alexander Richard, Dejan Markovic, Israel D Gebru, Steven Krenn, Gladstone Alexander Butler, Fernando Torre, and Yaser Sheikh. Neural synthesis of binaural speech from mono audio. In *Proceedings of the International Conference on Learning Representations (ICLR)*, 2021.

Edward B Saff and Amo B J Kuijlaars. Distributing many points on a sphere. *The Mathematical Intelligencer*, 19(1):5–11, 1997.

Ralph O Schmidt. Multiple emitter location and signal parameter estimation. *IEEE Transactions on Antennas and Propagation*, 34(3):276–280, 1986.

Ayal Schwartz, Elior Hadad, Sharon Gannot, and Shlomo E Chazan. Array configuration mismatch in deep DOA estimation: Towards robust training. In *Proceedings of the IEEE Workshop on Applications of Signal Processing to Audio and Acoustics (WASPAA)*, pp. 1–5, 2023.

Peter Shaw, Jakob Uszkoreit, and Ashish Vaswani. Self-attention with relative position representations. In *Proceedings of the Conference of the North American Chapter of the Association for Computational Linguistics (NACCL)*, pp. 464–468, 2018.

Bowen Shi, Wei-Ning Hsu, Kushal Lakhotia, and Abdelrahman Mohamed. Learning audio-visual speech representation by masked multimodal cluster prediction. In *Proceedings of the International Conference on Learning Representations (ICLR)*, 2022.

Kazuki Shimada, Archontis Politis, Parthasaarathy Sudarsanam, Daniel A Krause, Kengo Uchida, Sharath Adavanne, Aapo Hakala, Yuichiro Koyama, Naoya Takahashi, Shusuke Takahashi, Tuomas Virtanen, and Yuki Mitsufuji. STARSS23: An audio-visual dataset of spatial recordings of real scenes with spatiotemporal annotations of sound events. In *Proceedings of the Advances in Neural Information Processing Systems (NeurIPS)*, pp. 72931–72957, 2023.

Matthieu Simeoni, Sepand Kashani, Paul Hurley, and Martin Vetterli. DeepWave: A recurrent neural-network for real-time acoustic imaging. In *Proceedings of the Advances in Neural Information Processing Systems (NeurIPS)*, 2019.

Jianlin Su, Murtadha Ahmed, Yu Lu, Shengfeng Pan, Wen Bo, and Yunfeng Liu. RoFormer: Enhanced Transformer with rotary position embedding. *Neurocomputing*, 568:127063, 2024.

Peiwen Sun, Sitong Cheng, Xiangtai Li, Zhen Ye, Huadai Liu, Honggang Zhang, Wei Xue, and Yike Guo. Both ears wide open: Towards language-driven spatial audio generation. In *Proceedings of the International Conference on Representation Learning (ICLR)*, pp. 42606–42649, 2025.

Ashish Vaswani, Noam Shazeer, Niki Parmar, Jakob Uszkoreit, Llion Jones, Aidan N Gomez, Łukasz Kaiser, and Illia Polosukhin. Attention is all you need. In *Proceedings of the Advances in Neural Information Processing Systems (NeurIPS)*, pp. 5998–6008, 2017.

Jiadong Wang, Xinyuan Qian, Zihan Pan, Malu Zhang, and Haizhou Li. GCC-PHAT with speech-oriented attention for robotic sound source localization. In *Proceedings of the IEEE International Conference on Robotics and Automation (ICRA)*, pp. 5876–5883, 2021.

Jiang Wang, Yuanzheng He, Daobilige Su, Katsutoshi Itoyama, Kazuhiro Nakadai, Junfeng Wu, Shoudong Huang, Youfu Li, and He Kong. SLAM-based joint calibration of multiple asynchronous microphone arrays and sound source localization. *IEEE Transactions on Robotics*, 40: 4024–4044, 2024a.

Lin Wang and Andrea Cavallaro. Deep-learning-assisted sound source localization from a flying drone. *IEEE Sensors Journal*, 22(21):20828–20838, 2022.

Yabo Wang, Bing Yang, and Xiaofei Li. IPDnet: A universal direct-path IPD estimation network for sound source localization. *IEEE/ACM Transactions on Audio, Speech, and Language Processing*, 32:5051–5064, 2024b.

Deyun Wei and Jun Yang. Non-uniform sparse Fourier transform and its applications. *IEEE Transactions on Signal Processing*, 70:4468–4482, 2022.

Muqian Wen and John Houlihan. Application of the non-uniform Fourier transform to non-uniformly sampled Fourier transform spectrometers. *Optics Communications*, 540:129491, 2023.

Jiajian Xie, Shengyu Zhang, Mengze Li, chengfei lv, Zhou Zhao, and Fei Wu. EcoFace: Audio-visual emotional co-disentanglement speech-driven 3D talking face generation. In *Proceedings of the International Conference on Learning Representations (ICLR)*, pp. 101625–101643, 2025.

Zhongweiyang Xu, Xulin Fan, Zhong-Qiu Wang, Xilin Jiang, and Romit Roy Choudhury. Array-DPS: Unsupervised blind speech separation with a diffusion prior. In *Proceedings of the International Conference on Machine Learning (ICML)*, pp. 69160–69188, 2025.

Bing Yang, Hong Liu, and Xiaofei Li. Learning deep direct-path relative transfer function for binaural sound source localization. *IEEE/ACM Transactions on Audio, Speech, and Language Processing*, 29:3491–3503, 2021.

Yufeng Yang, Desh Raj, Ju Lin, Niko Moritz, Junteng Jia, Gil Keren, Egor Lakomkin, Yiteng Huang, Jacob Donley, Jay Mahadeokar, and Ozlem Kalinli. M-BEST-RQ: A multi-channel speech foundation model for smart glasses. In *Proceedings of the IEEE International Conference on Acoustics, Speech and Signal Processing (ICASSP)*, pp. 1–5, 2025.

Takuya Yoshioka, Xiaofei Wang, Dongmei Wang, Min Tang, Zirun Zhu, Zhuo Chen, and Naoyuki Kanda. VarArray: Array-geometry-agnostic continuous speech separation. In *Proceedings of the IEEE International Conference on Acoustics, Speech and Signal Processing (ICASSP)*, pp. 6027–6031, 2022.

Dehao Zhang, Shuai Wang, Ammar Belatreche, Wenjie Wei, Yichen Xiao, Haorui Zheng, Zijian Zhou, Malu Zhang, and Yang Yang. Spike-based neuromorphic model for sound source localization. In *Proceedings of the Advances in Neural Information Processing Systems (NeurIPS)*, pp. 113911–113936, 2024.

Yue Zhang, Zhiyang Xu, Ying Shen, Parisa Kordjamshidi, and Lifu Huang. SPARTUN3D: Situated spatial understanding of 3D world in large language model. In *Proceedings of the International Conference on Learning Representations (ICLR)*, pp. 73388–73406, 2025.

Zhisheng Zheng, Puyuan Peng, Ziyang Ma, Xie Chen, Eunsol Choi, and David Harwath. BAT: Learning to reason about spatial sounds with large language models. In *Proceedings of the International Conference on Machine Learning (ICML)*, pp. 61454–61469, 2024.

Yongchao Zhou, Uri Alon, Xinyun Chen, Xuezhi Wang, Rishabh Agarwal, and Denny Zhou. Transformers can achieve length generalization but not robustly. In *Proceedings of the International Conference on Learning Representations Workshop on Mathematical and Empirical Understanding of Foundation Models*, 2024.

Qiushi Zhu, Jie Zhang, Yu Gu, Yuchen Hu, and Lirong Dai. Multichannel AV-wav2vec2: A framework for learning multichannel multi-modal speech representation. In *Proceedings of the AAAI Conference on Artificial Intelligence*, pp. 19768–19776, 2024.

A Appendix

A.1 Relationship between TDOA and Relative Microphone Positions

We derive here the relationship between the TDOA and relative microphone positions under the standard plane-wave assumption. Assuming a far-field source, the time of arrival $\tau(\cdot)$ at a microphone position $\mathbf{p} \in \mathbb{R}^3$ is given by

$$\tau(\mathbf{p}) = \tau_0 - \frac{\mathbf{u}^\top \mathbf{p}}{v}, \tag{17}$$

where τ_0 is the reference arrival time at the origin of the coordinates, $\mathbf{u} \in \mathbb{R}^3$ is the unit direction vector of the incoming wave, and v is the speed of sound. Let $\mathbf{p}_m$ and $\mathbf{p}_n$ denote the positions of the m-th and n-th microphones, respectively. Their TDOA $\Delta\tau_{m,n}$ is

$$\Delta\tau_{m,n} = \tau(\mathbf{p}_m) - \tau(\mathbf{p}_n) = \frac{\mathbf{u}^\top(\mathbf{p}_n - \mathbf{p}_m)}{v} = \frac{\mathbf{u}^\top \Delta\mathbf{p}_{m,n}}{v}, \tag{18}$$

where $\Delta\mathbf{p}_{m,n} := \mathbf{p}_n - \mathbf{p}_m$ is the relative microphone position vector. This result shows that the TDOA depends solely on the relative microphone positions $\Delta\mathbf{p}_{m,n}$, which is analogous to Eq. (10), not on their absolute coordinates. As the IPD is given by $\Delta\theta_{m,n}(f) = 2\pi f\, \Delta\tau_{m,n}$, the same property holds for IPDs as well. Therefore, encoding microphone geometry in a relative form, as done in the proposed rMPE, is directly grounded in the underlying physics of wave propagation.

A.2 LNuDFT Parameter Visualization

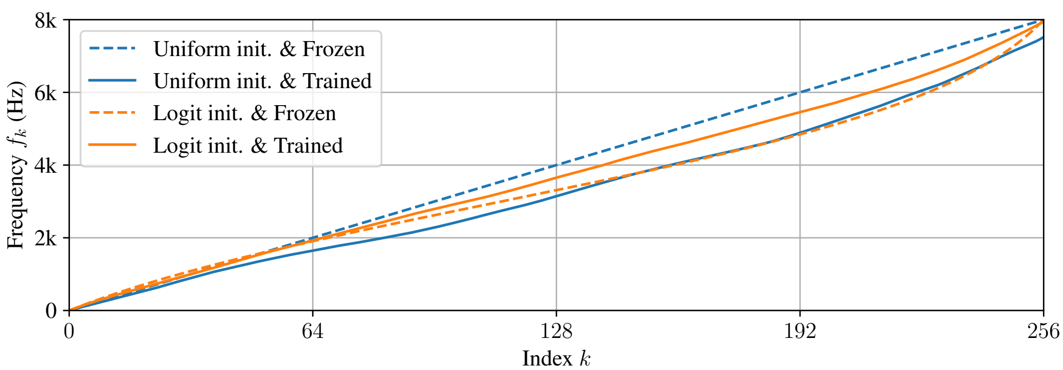

Figure 3: Frequency response of LNuDFT parameters.

Figure 3 shows the frequency response of the LNuDFT parameters with $f_k = \frac{\nu_k}{N} f_s$, where the sampling frequency was $f_s = 16$ kHz. The horizontal axis represents the indices of the LNuDFT parameters, k, and the vertical axis represents the frequency f_k in Hz. The standard DFT was initialized with uniformly spaced bins, which after training evolved into a non-uniform spacing that allocates higher resolution to the 1.5–7.5 kHz range. In contrast, the proposed logit-based initialization already placed parameters densely within the 2–6 kHz region at initialization, and they tended to evolve toward a more uniform spacing after training. This behavior indicates that the model tended to attenuate resolution at too low and high frequencies, concentrating more bins in the mid-frequency range. It denotes that the proposed initialization and the results of LNuDFT were well aligned with the spectral characteristics of speech signals, which are primarily concentrated in this frequency range, and provides informative IPD cues crucial for SSL and TDOA estimation.

The selected values of $\epsilon_{\text{start}} = 0.15$ and $\epsilon_{\text{end}} = 0.95$ for the logit-based initialization were chosen to assign denser sampling to the low- and mid-frequency regions, while sparsely covering the high-frequency region to avoid spatial aliasing. As shown in Fig. 3, this initialization results in frequency allocations that concentrate primarily on the mid-frequency bins where IPD cues are most reliable. Furthermore, the initialization also assigned slightly denser sampling in the low-frequency bins than in the high-frequency bins, ensuring stable IPD information while avoiding aliasing effects. We performed a grid search over ϵ_{start} and ϵ_{end} and observed that small perturbations around the selected values did not significantly affect performance. The chosen configuration provided the most consistent and robust results across our experiments.

A.3 AuGeonet Architecture

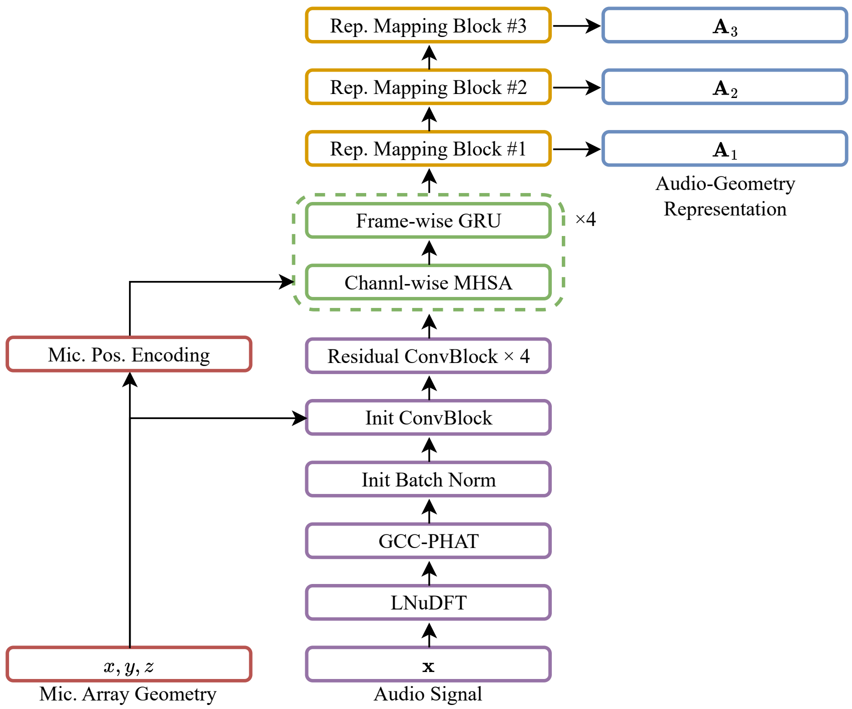

Figure 4: AuGeonet architecture.

The overall structure of AuGeonet is modified from GI-DOAEnet (Baek et al., 2025), with detailed architecture available in the original paper. The default settings of the AuGeonet were $M = 128$, $\alpha = 7$, $\beta = 4$, $O = 3$, and $G = 256$. Other hyperparameters followed those of GI-DOAEnet. Figure 4 illustrates the modified AuGeonet architecture, and the key modifications are summarized below:

- **Input feature.** The input is replaced with LNuDFT-based GCC-PHAT features.
- **Integrating the geometry information.** Each channel of the input GCC-PHAT features are treated as a batch. These features are first processed with 1D batch normalization (BN) (Ioffe & Szegedy, 2015), and relative microphone coordinates in both Cartesian and sinusoidal spherical forms $(\tilde{x}_c, \tilde{y}_c, \tilde{z}_c, \tilde{r}_c, \sin\tilde{\vartheta}_c, \cos\tilde{\vartheta}_c, \sin\tilde{\varphi}_c, \cos\tilde{\varphi}_c)$ from Eq. (10) are concatenated along the frequency dimension to provide comprehensive geometry information. Then, an initial ConvBlock (CB), consisting of an 1D convolution layer, an ELU (Clevert et al., 2016) activation, and a BN, projects the frequency dimension from $2K+8$ to feature size M. A stack of Residual ConvBlocks (RCBs), each composed of two CBs with a residual connection, follows the initial CB to extract local features. rMPE is added to the input of each RCB, and a total of 4 RCBs are used.

  After the RCBs, four spatio-temporal dual-path blocks (STDPBs) are applied. Each STDPB consists of a CW-MHSA with rMPE, which captures spatial dependencies by applying MHSA across the channel dimension for each time frame, and a frame-wise GRU (Cho et al., 2014), which models temporal dependencies.
- **Output representation.** Finally, O representation mapping blocks (RMBs) are used instead of the spatial spectrum mapping blocks in GI-DOAEnet. Each RMB consists of an RCB, which applies LN instead of BN, followed by a linear layer that projects the features to size G. The output of RCB each RMB is also passed to the subsequent one.

A.4 Gridnet Architecture

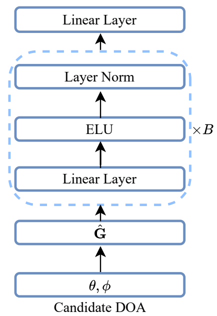

Figure 5: Gridnet architecture.

Gridnet consists of B sequential blocks, each composed of a linear layer that preserves the feature dimension G, followed by an ELU activation (Clevert et al., 2016) and a layer normalization (LN) (Ba et al., 2016) layer, as illustrated in Fig. 5. A final linear layer produces the output, GR. All candidate DOAs are modulated with sinusoidal encoding before being input to Gridnet. These modulated candidate DOAs are processed in batch, allowing Gridnet to efficiently handle varying numbers of candidates D without retraining. B was set to 3, and the frequency modulation factor ξ was set to 1 in our experiments.

A.5 Fibonacci Sphere Sampling

Algorithm 1: Fibonacci Sphere Point Generation

Input: Number of DOA grids D

Output: Set of 3D points $\mathbf{\Psi} = \{\psi_d\}_{d=0}^{D-1},\ \psi_d = (x_d, y_d, z_d, \theta_d, \phi_d) \in \mathbb{R}^3$ on the unit sphere

$\varphi \leftarrow \frac{1+\sqrt{5}}{2}$

$\vartheta \leftarrow \frac{2\pi}{\varphi}$

for $d \leftarrow 0$ **to** $D-1$ **do**

  $z \leftarrow 1 - \frac{2d+1}{D}$

  $r \leftarrow \sqrt{1-z^2}$

  $\omega \leftarrow d \cdot \vartheta$

  $x \leftarrow r\cos\omega$

  $y \leftarrow r\sin\omega$

  $\theta \leftarrow \mathrm{atan2}(y, x)$

  $\phi \leftarrow \frac{\pi}{2} - \mathrm{atan2}(z, \sqrt{x^2+y^2})$

  Add point $\psi_d = (x, y, z, \theta, \phi)$ to $\mathbf{\Psi}$

end

return $\mathbf{\Psi}$

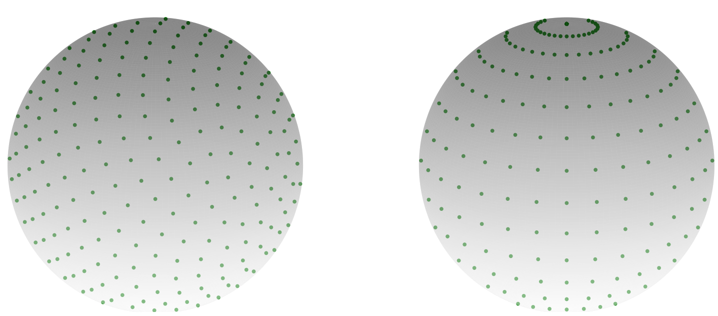

(a) Fibonacci sphere sampling. (b) Equiangular sphere sampling.

Figure 6: Examples of (a) Fibonacci sphere sampling and (b) equiangular sphere sampling.

Fibonacci sphere sampling generates nearly uniform points on the unit sphere using the golden angle, thereby avoiding the pole clustering problem of latitude–longitude grids (Saff & Kuijlaars, 1997). Algorithm 1 summarizes the procedure, with φ denoting the golden ratio. Figure 6(a) shows an example with $D = 512$ points, while Fig. 6(b) illustrates equiangular sampling (32 azimuth $\times$ 16 elevation), which suffers from dense clustering at the poles. This method efficiently approximates uniform sampling without complex computations.

A.6 Oracle Spatial Spectrum Generation

The oracle spatial spectrum $\mathbf{S} \in \mathbb{R}^{D\times O\times L}$ is generated as:

$$\mathbf{S}_{d,o,l} = \begin{cases} \max\limits_{\psi_l \in \Psi_l} \left\{ e^{\kappa(\gamma_o)\left(\cos\left(\delta(\varsigma_d,\psi_l)\right)-1\right)} \right\}, & \text{if } |\Psi_l| > 0, \\ 0, & \text{otherwise,} \end{cases} \tag{19}$$

$$\delta(\varsigma,\psi) = \arccos\left(x_\varsigma x_\psi + y_\varsigma y_\psi + z_\varsigma z_\psi\right), \tag{20}$$

$$\kappa(\gamma) = \frac{-\ln\sqrt{2}}{\cos\gamma - 1}, \tag{21}$$

where Ψ_l is the set of ground-truth DOAs at the l-th frame, and ς_d is the d-th DOA candidate. The angular distance between a candidate and a ground-truth DOA is computed by $\delta(\cdot)$, and γ_o controls the beamwidth (Choi & Chang, 2022) for the o-th output. A smaller γ_o yields narrower beams with sharper peaks but weaker relationships across neighboring DOAs, while a larger γ_o produces wider beams with smoother transitions.

A.7 Loss Function

The weighted BCE loss is defined as:

$$\mathcal{L}(\mathbf{S},\hat{\mathbf{S}}) = -\frac{1}{L\cdot D}\sum_{o=1}^{O}\sum_{l=1}^{L}\sum_{d=1}^{D}\left\{\rho\cdot\mathbf{S}_{d,o,l}\log\hat{\mathbf{S}}_{d,o,l} + (1-\mathbf{S}_{d,o,l})\log\left(1-\hat{\mathbf{S}}_{d,o,l}\right)\right\}, \tag{22}$$

where ρ is a weighting factor to balance the loss between positive (ground-truth DOAs) and negative samples (Nguyen et al., 2020). In our experiments, we set $\rho = 2$.

A.8 Iterative Max-Peak Selection Algorithm

Algorithm 2: Iterative max-peak selection from spatial spectrum

Input: Predicted spatial spectrum $\hat{\mathbf{S}}_{o,l}$, number of active speakers T_l, angular distance margin $\bar{L}$
Output: Set of estimated DOAs $\hat{\Psi}_l$
Initialize $\hat{\Psi}_l \leftarrow \emptyset$
while $|\hat{\Psi}_l| < T_l$ **do**
    Find index $d^* \leftarrow \arg\max_d \hat{\mathbf{S}}_{d,o,l}$
    Add DOA candidate ψ_{d^*} to $\hat{\Psi}_l$
    Suppress $\hat{\mathbf{S}}_{d,o,l} \leftarrow 0$ for all d within angular distance $\bar{L}$ of d^* (computed using Eq. (20)).
return $\hat{\Psi}_l$

Algorithm 2 outlines the iterative max-peak selection method for estimating DOAs (Baek et al., 2023) from the predicted spatial spectrum $\hat{\mathbf{S}}_{o,l} \in \mathbb{R}^D$, where D is the number of candidate points at the l-th frame and o-th output. The number of active speakers T_l is assumed to be known a priori, and $\bar{L}$ is an angular distance margin to avoid selecting multiple peaks from the same source, which was set to 10° in our experiments.

A.9 Model Training Details

Every DNN-based method used similar training settings. The batch size was set to 16 for most models, except Neural-SRP which reduced to 1 due to memory constraints of GPU. All models were implemented in PyTorch and trained on a single NVIDIA RTX 3090 / 4090 GPU. We used the weighted BCE loss in Eq. (22), and the Adam optimizer (Kingma & Ba, 2014), gradient clipping within 1, and an adaptive learning rate schedule that decayed by 0.9 if the validation loss did not improve for two consecutive epochs. To facilitate robust SSL learning, we employed complexity gradual training (CGT) strategy (Baek et al., 2025), consisting of multi-stage geometry learning (MSGL) and DSCL.

Table 6: Multi-stage geometry learning (MSGL) hyperparameters.

Stage	Microphone Array	Number of channels	Learning Rate	Weight Decay	Epoch
1	Tetrahedron (4 cm)	4	2.5×10^{-4}	1.0×10^{-4}	1–10
2	Dynamic	4	5.0×10^{-4}	1.0×10^{-6}	11–20
3	Dynamic	4–12	1.0×10^{-3}	1.0×10^{-6}	21–300

Table 6 summarizes the MSGL setup. The training complexity was gradually increased: from fixed to dynamic MAs, and from a fixed to variable number of channels, with stage-specific learning rates and weight decay for stable convergence. Each epoch contained 28,800 utterances for training, and validation was conducted after every epoch (2,000 samples in stages 1–2, and 300 samples per channel in stage 3). DSCL employed multiple outputs with varying beamwidth targets, starting coarse and gradually refining them. Beamwidth parameters γ_o were initialized as $[32°, 12°, 5°]$ and decreased linearly to $[5°, 5°, 5°]$ between epochs 35–60. This coarse-to-fine scheme first captures broad spatial patterns and then sharpens them into accurate spatial spectra for SSL.

A.10 Synthetic Dataset Generation

Algorithm 3: Synthetic dataset generation.

Input: Anechoic speech dataset, noise dataset, number of channels C
Output: Synthetic mixtures, oracle voice activity detection (VAD) labels, ground-truth DOAs
foreach *utterance* **do**

- **Speech selection:** Randomly select speakers and utterances, resample to 16 kHz, trim/pad to 4 s, and obtain oracle VAD labels using WebRTC VAD[a].
- **Noise generation:** Select one coherent noise, resample to 16 kHz, generate channel-wise Gaussian white noise, and trim/pad to 4 s.
- **Spatial setup:** Randomly configure room size, RT60, and C-channel 3D geometry with inter-microphone distances constrained by Eq. (23). Place speakers with at least 10° angular separation, with coherent noise placed at least 2.5 m away, and ensure the microphone array is at least 0.1 m from walls.
- **RIR generation:** Generate synthetic RIRs using gpuRIR (Diaz-Guerra et al., 2021b) with the image source method (Allen & Berkley, 1979) and diffuse modeling.
- **Signal construction:** Convolve signals with RIRs, mix speech with random SIR, mix noises with random SIR, and combine speech and noise with random SNR.

[a] `https://github.com/wiseman/py-webrtcvad`

$$\begin{aligned} R_{\text{min}} &= \left[\max\left(1,\, 4-3\cdot\tfrac{C-4}{8}\right),\, 6\right]\ \text{cm}, \\ R_{\text{max}} &= \left[7,\, \max\left(7,\, 9+4\cdot\tfrac{C-4}{8}\right)\right]\ \text{cm}. \end{aligned} \tag{23}$$

This section details the process of generating the synthetic dataset, following the procedure of Baek et al. (2025). Algorithm 3 outlines the steps, while Eq. (23) defines the minimum R_{min} and maximum R_{max} inter-microphone distances as a function of the number of channels C. Table 1 summarizes the ranges of acoustic parameters used in Algorithm 3 for generating the synthetic dataset. Each parameter was randomly sampled from a uniform distribution within the specified interval, except for the elevation angle. The elevation was drawn from a von Mises-Fisher distribution (Fisher et al., 1993), given by $\frac{\varphi}{2}$, where $\varphi \sim \text{vMF}(\mu, \kappa)$ with $\mu = \pi$ and $\kappa = 2$, favoring positions near the horizontal plane while restricting the range to $[0, \pi]$.

For training and validation, anechoic utterances were taken from LibriSpeech (Panayotov et al., 2015), where the `train-clean-100` and `test-clean` sets were used, respectively, and noises were taken from MS-SNSD (Reddy et al., 2019), where the `train` and `test` sets were used, respectively. Anechoic speech for evaluation was taken from TIMIT (Garofolo et al., 1993), and noises from ESC-50 (Piczak, 2015).

A.11 Evaluation Metrics

MAE (°) and ACC_{10} (%) are defined as:

$$\mathrm{MAE}\,(^\circ) = \frac{180}{\pi}\frac{1}{|\mathbf{L}_{\mathrm{act}}|}\sum_{l\in\mathbf{L}_{\mathrm{act}}}\frac{1}{T_l}\min_{p\in P_l}\sum_{s=1}^{T_l}\delta\left(\varsigma_s, \hat{\psi}_{p(s)}\right), \tag{24}$$

$$\mathrm{ACC}_{10}(\%) = \frac{|\mathbf{L}_{\mathrm{acc}}|}{|\mathbf{L}_{\mathrm{act}}|}\times 100, \tag{25}$$

where $|\cdot|$ denotes the cardinality of a set, and $\mathbf{L}_{\mathrm{act}}$ is the set of active speaker labels in the utterance. T_l is the number of sources for the l-th frame, P_l is the set of all permutations of T_l sources, ς_s is the ground-truth DOA of source s, $\hat{\psi}_{p(s)}$ is the estimated DOA assigned to source s under permutation p, and $\delta(\cdot)$ is the angular distance between two directions computed using Eq. (20). MAE computes the mean angular error between ground-truth and estimated DOAs, considering all possible source permutations to resolve permutation ambiguity in multi-source scenarios. $\mathbf{L}_{\mathrm{acc}}$ is the subset of $\mathbf{L}_{\mathrm{act}}$ whose angular error is less than 10°.

A.12 Box and Violin Plots of the Results

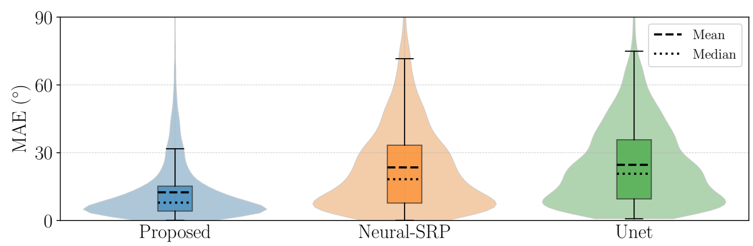

Figure 7: Box and violin plots of MAE for *Dynamic-S* with 4–12 channels.

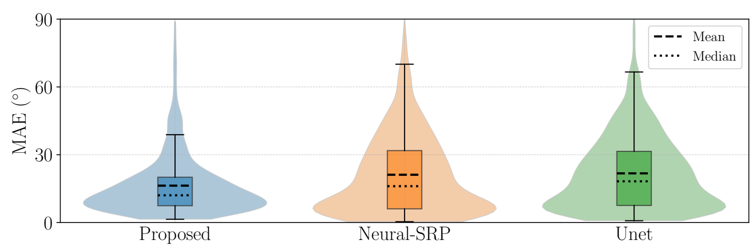

Figure 8: Box and violin plots of MAE for *Dynamic-U* with 13–16 channels.

Figures 7 and 8 present the box and violin plots of MAE results for *Dynamic-S* with 4–12 channels and *Dynamic-U* with 13–16 channels, respectively. Box plots show the interquartile range (IQR), and whiskers, where the black solid line denotes whiskers within 1.5 times the IQR. The dotted and dashed lines inside box plots indicate the median and mean of each method, respectively. Violin plots illustrate the kernel density estimation of the distribution. The proposed method exhibited a more pronounced peak around the median values with a narrower distribution, indicating that the results were more concentrated and consistent compared to the baselines, Unet and Neural-SRP, both equipped with AGG-RL.

A.13 Analysis Across Environmental Conditions

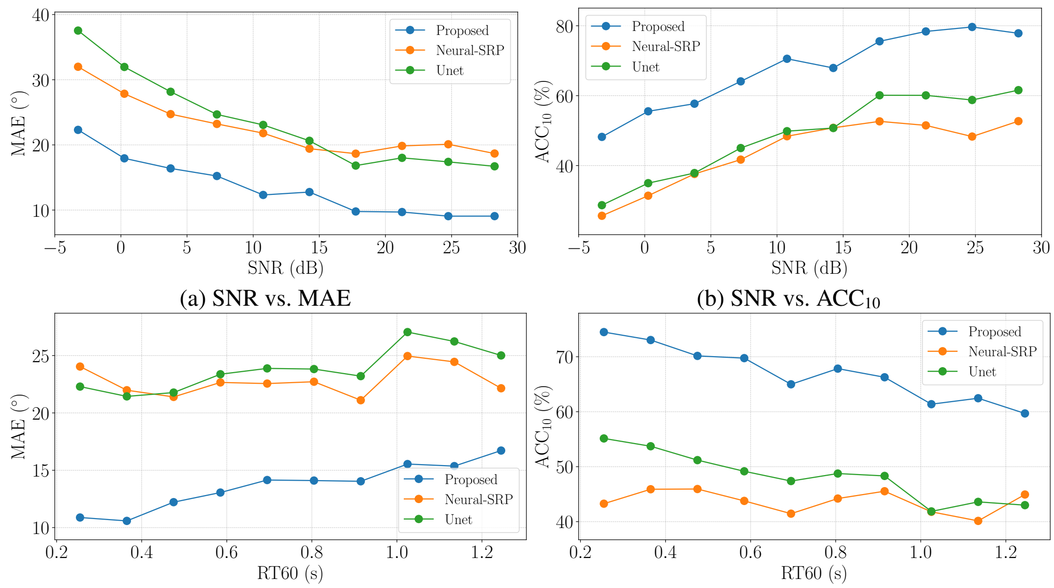

(a) SNR vs. MAE

(b) SNR vs. ACC_{10}

(c) RT60 vs. MAE

(d) RT60 vs. ACC_{10}

Figure 9: MAE and ACC_{10} results of the proposed method and baselines (Unet, Neural-SRP; both with AGG-RL) on the *Dynamic-S* and *Dynamic-U* datasets across different SNR and RT60 conditions.

To assess the impact of environmental conditions on SSL performance, we analyzed the results across varying SNRs and RT60s using the synthetic datasets. Figure 9 illustrates the MAE and ACC_{10} results for *Dynamic-S* and *Dynamic-U*, comparing the proposed method with the baselines (Unet and Neural-SRP), both equipped with AGG-RL. The two datasets were combined to provide a comprehensive overview of performance tendencies under varying environmental conditions. The combined datasets were divided into 10 equally sized bins for each SNR and RT60 range, and the nearest values to the bin centers were averaged. All methods showed improved performance with increasing SNR and decreasing RT60, as easier acoustic conditions inherently facilitate more accurate SSL. Notably, the proposed method consistently outperformed the baselines across all SNR and RT60 ranges, demonstrating strong robustness under both low-SNR and highly reverberant conditions.

Table 7: Experimental results under different numbers of active speakers across all datasets.

	NAO robot		*Eigenmike*		*Dynamic-S*		*Dynamic-U*	
	MAE	ACC_{10}	MAE	ACC_{10}	MAE	ACC_{10}	MAE	ACC_{10}
Unet								
1 speaker	11.59 $\pm$3.43	93.00	16.14 $\pm$3.69	68.49	16.92 $\pm$0.91	62.74	13.52 $\pm$1.20	71.68
2 speakers	19.78 $\pm$5.74	24.41	23.29 $\pm$4.75	12.14	32.46 $\pm$0.84	29.76	30.06 $\pm$1.14	33.98
Neural-SRP								
1 speaker	7.28 $\pm$2.62	90.21	10.77 $\pm$2.28	79.08	12.77 $\pm$0.84	63.65	9.73 $\pm$0.97	73.21
2 speakers	13.28 $\pm$5.31	33.74	17.89 $\pm$3.67	17.24	33.55 $\pm$0.93	20.92	31.22 $\pm$1.30	26.47
Proposed								
1 speaker	7.48 $\pm$1.54	96.06	9.77 $\pm$1.42	81.13	7.08 $\pm$0.52	85.95	9.51 $\pm$0.92	74.09
2 speakers	10.71 $\pm$3.54	73.90	15.93 $\pm$3.56	43.50	17.93 $\pm$0.73	58.84	21.17 $\pm$1.10	39.58

Table 7 summarizes the experimental results under different numbers of active speakers across all datasets. All methods showed degradation when moving from one to two speakers, which reflects the increased difficulty of SSL in multi-source scenarios. However, except for the MAE in the single-speaker condition of the *NAO robot* dataset—where Neural-SRP showed marginally better performance—the proposed method consistently outperformed both baselines across all datasets and speaker configurations, demonstrating its strong ability to handle both single- and multi-speaker spatial scenes.

A.14 RESULTS WITH STARSS23 DATASET

Table 8: Experimental results on *STARSS23* with different methods. The best results on each dataset are in **bold**.

	Total		1 Speaker		2 Speakers	
	MAE	ACC_{10}	MAE	ACC_{10}	MAE	ACC_{10}
Unet	43.91 $\pm$4.97	23.55	38.37 $\pm$8.55	35.71	46.03 $\pm$5.96	18.90
Neural-SRP	55.54 $\pm$7.55	5.74	50.11 $\pm$16.56	10.12	57.62 $\pm$8.35	4.07
Proposed	**27.32** $\pm$5.50	**36.09**	**18.67** $\pm$6.15	**56.58**	**30.63** $\pm$6.96	**28.25**

For further validation, we evaluated the proposed method using the *STARSS23* dataset (Shimada et al., 2023), which consists of real-recorded multi-speaker reverberant mixtures originally recorded with a 32-channel Eigenmike MA. The official dataset provides downmixed versions using 6-, 10-, 26-, and 22-th channel subsets, corresponding to a 4-channel tetrahedral-shape configuration. Although the dataset was developed for sound event localization and detection (SELD), we focused exclusively on the speech localization aspect. Speech-only segments were selected based on the provided annotations. The results in Table 8 show a noticeable degradation compared to Table 3. This is expected because *STARSS23* involves low SNR conditions with various sound events, highly dynamic scenes with moving speakers, and acoustic characteristics that differ significantly from our static, synthetic training data. Despite these challenges, the proposed method consistently outperformed the baselines across all evaluation settings, demonstrating strong generalization capability to real-world and dynamic recording conditions.

A.15 Spatial Spectrum Visualization

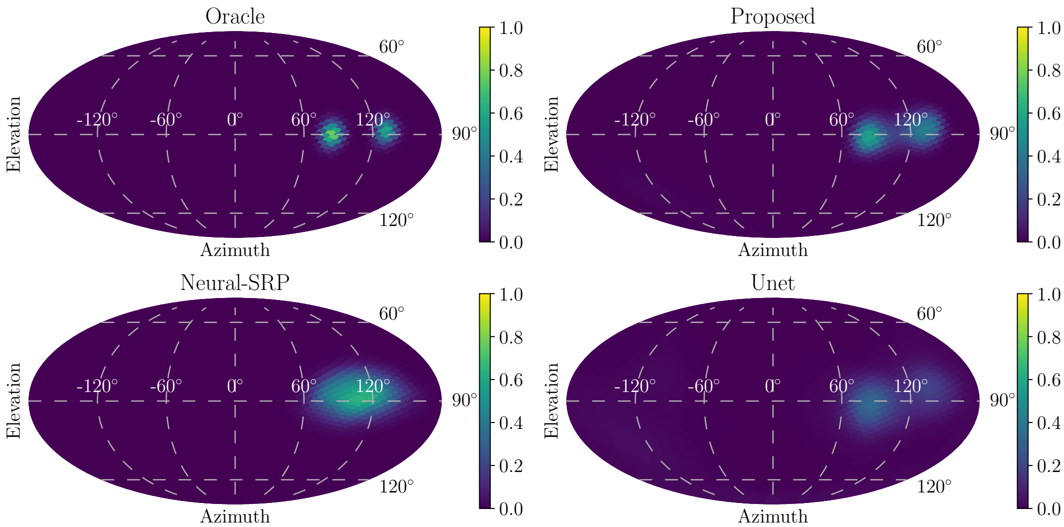

Figure 10: Spatial spectra averaged across frames for an utterance with two active speakers from the *NAO robot* dataset, visualized in Mollweide projection. Peaks correspond to estimated DOAs on the unit sphere.

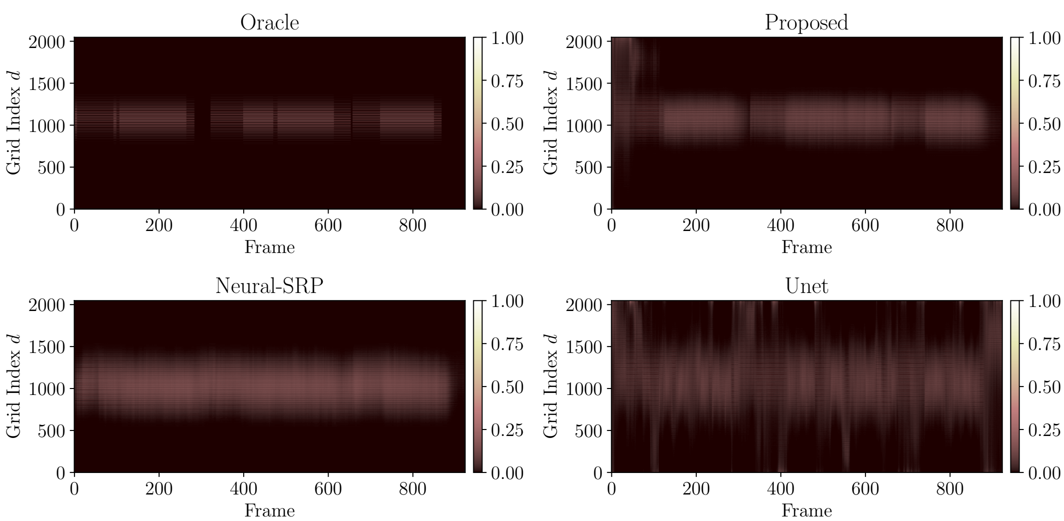

Figure 11: Frame-wise spatial spectra for the same utterance of Fig. 10, shown in 2D where the x-axis represents time frames and the y-axis denotes grid indices.

Figure 10 illustrates the spatial spectra of the oracle, the proposed method, Neural-SRP, and Unet on an utterance with two active speakers from the *NAO robot* dataset. For visualization, frame-level spectra were averaged and projected onto the Mollweide map. The proposed method produced sharp and distinct peaks exactly at both ground-truth DOAs, closely resembling the oracle. In contrast, Neural-SRP yielded a broad peak that failed to clearly separate the two speakers, while Unet generated less distinctive peaks. Figure 11 illustrates the spatial spectra in 2D, where x- and y-axis represent frame and DOA index d, respectively. The proposed method consistently produced stable peaks aligned with ground-truth DOAs and accurate VAD estimation, whereas Neural-SRP and Unet exhibited less consistent activations and unreliable VAD distinction.

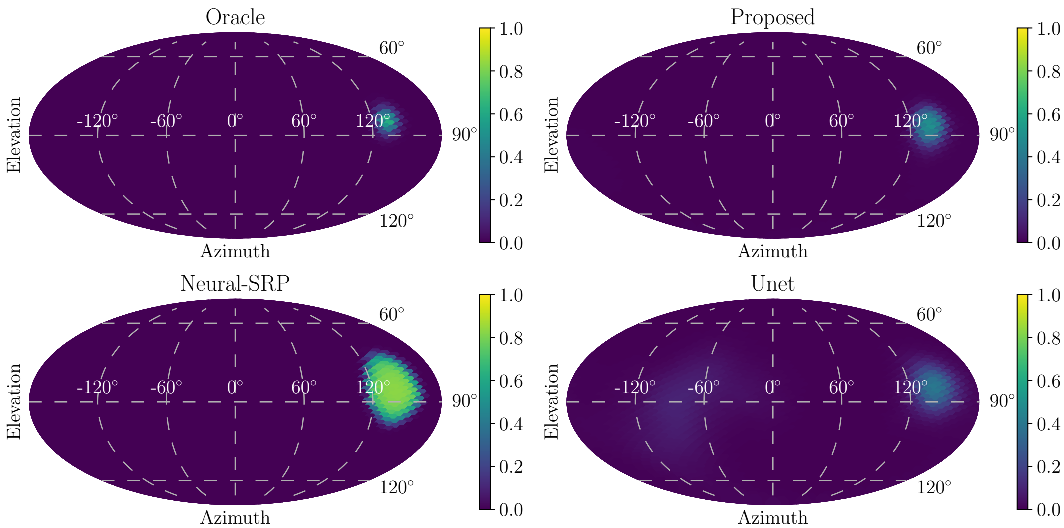

Figure 12: Spatial spectra averaged across frames for an utterance with a single active speaker from the *Eigenmike* dataset, visualized in Mollweide projection. Peaks correspond to estimated DOAs on the unit sphere.

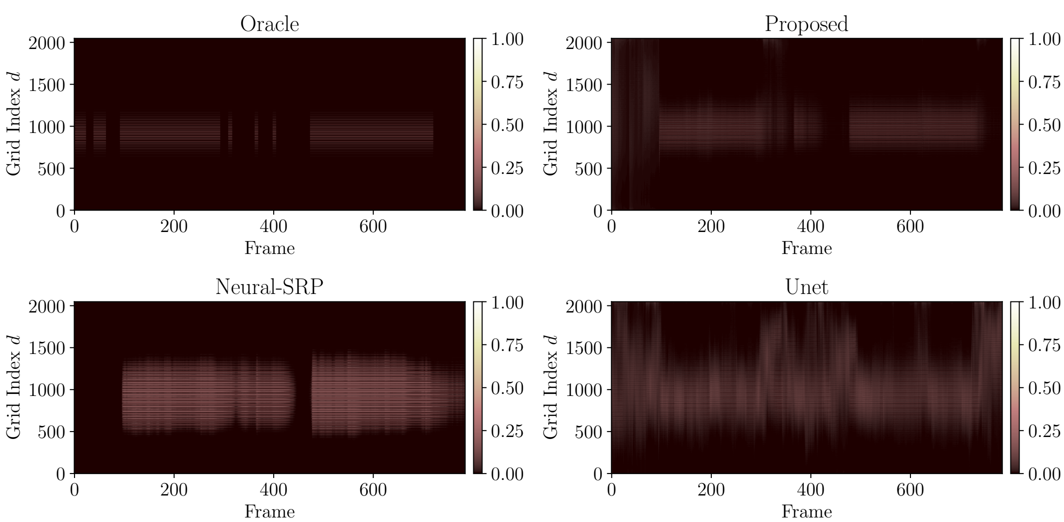

Figure 13: Frame-wise spatial spectra for the same utterance of Fig. 12, shown in 2D where the x-axis represents time frames and the y-axis denotes grid indices.

Figures 12 and 13 show the spatial spectra of the oracle, proposed method, Neural-SRP, and Unet on an utterance with a single active speaker from the *Eigenmike* dataset, using Mollweide projection and 2D frame-wise view, respectively. In the Mollweide projection (Fig. 12), the proposed method produced a distinct and sharp peak at the ground-truth DOA. By contrast, Neural-SRP yielded a broad peak that did not clearly indicate the source location, while Unet produced multiple non-ground-truth peaks (e.g., near -90° azimuth), demonstrating less reliable estimation. In the 2D representation (Fig. 13), the proposed method consistently localized the source with sharp peaks and reliable VAD, closely matching the oracle. Neural-SRP again exhibited a wide, ambiguous peak, and Unet generated less sharp peaks along with spurious responses. Overall, the proposed method yielded sharper and more stable spatial spectra than the baselines, highlighting its robustness for unseen MA geometries.

A.16 VISUALIZATION OF GRID REPRESENTATIONS

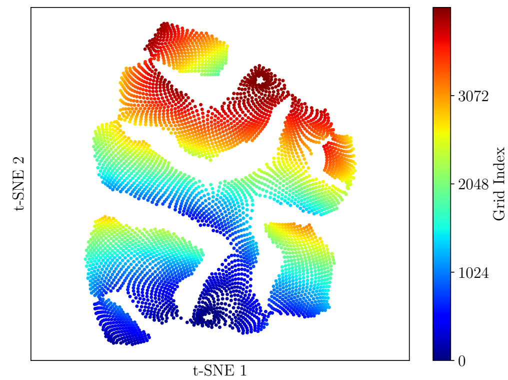

Figure 14: Grid representations visualized with t-SNE. Fibonacci grid points with $D = 4096$ are used as input candidates.

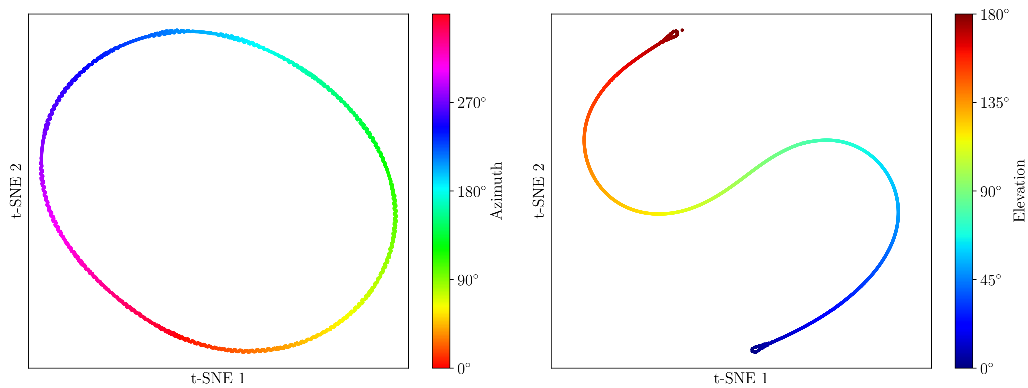

(a) t-SNE with varying azimuth

(b) t-SNE with varying elevation

Figure 15: Grid representations visualized with t-SNE for azimuth and elevation candidates.

Figure 14 visualizes the output with Fibonacci grid points with $D = 4096$. Nearby directions in 3D space were embedded closely, whereas opposite directions were mapped farther apart, demonstrating that the GRs preserved directional similarity in the latent space. Figure 15(a) illustrates the case of varying azimuth while fixing elevation at $90°$ with $D = 2048$. The t-SNE outputted form a circular pattern consistent with azimuthal changes, indicating smooth representation of angular variation. Figure 15(b) shows the case of varying elevation while fixing azimuth at $0°$ with $D = 2048$. The t-SNE outputted form an S-shaped pattern aligned with elevation changes, demonstrating that the Gridnet consistently encodes variations in elevation. These results indicate that Gridnet captured and preserved the relationships of candidate DOAs in the latent space, supporting flexible and interpretable candidate DOA representation.

A.17 THE USE OF LARGE LANGUAGE MODELS

The authors used large language models (LLMs) to assist in writing the manuscript, including refining language, and ensuring clarity and coherence.